

Last modified: April 30, 2021

---

# Electrode pooling: boosting the yield of extracellular recordings with switchable silicon probes

Kyu Hyun Lee<sup>1,†</sup>, Yu-Li Ni<sup>1,†</sup>, Jennifer Colonell<sup>2</sup>, Bill Karsh<sup>2</sup>, Jan Putzeys<sup>3</sup>, Marius Pachitariu<sup>2</sup>, Timothy D. Harris<sup>2</sup>, and Markus Meister<sup>1,\*</sup>

<sup>1</sup>Division of Biology and Biological Engineering, Caltech

<sup>2</sup>HHMI Janelia Research Campus

<sup>3</sup>IMEC, Leuven, Belgium

\*Corresponding author: [meister@caltech.edu](mailto:meister@caltech.edu)

<sup>†</sup>These authors contributed equally to this work.

## Abstract

State-of-the-art silicon probes for electrical recording from neurons have thousands of recording sites. However, due to volume limitations there are typically many fewer wires carrying signals off the probe, which restricts the number of channels that can be recorded simultaneously. To overcome this fundamental constraint, we propose a novel method called *electrode pooling* that uses a single wire to serve many recording sites through a set of controllable switches. Here we present the framework behind this method and an experimental strategy to support it. We then demonstrate its feasibility by implementing electrode pooling on the Neuropixels 1.0 electrode array and characterizing its effect on signal and noise. Finally we use simulations to explore the conditions under which electrode pooling saves wires without compromising the content of the recordings. We make recommendations on the design of future devices to take advantage of this strategy.

## 1 Introduction

Understanding brain function requires monitoring the complex pattern of activity distributed across many neuronal circuits. To this end, the BRAIN Initiative has called for the development of technologies for recording “dynamic neuronal activity from complete neural networks, over long periods, in all areas of the brain”, ideally “monitoring all neurons in a circuit” (BRAIN Working Group, 2014). Recent advances in the design and manufacturing of silicon-based neural probes have answered this challenge with new devices that have thousands of recording sites (Jun et al., 2017b; Dimitriadis et al., 2018; Rios et al., 2016; Torfs et al., 2010; Steinmetz et al., 2021). Still, the best methods sample neural circuits very sparsely, for example recording fewer than  $10^4$  cells in a mouse brain that has  $10^8$  (Stevenson, 2013).

In many of these electrode array devices only a small fraction of the recording sites can be used at once. The reason is that neural signals must be brought out of the brain via wires, which take up much more volume than the recording sites themselves. For example, in one state-of-the-art silicon shank, each wire displaces thirty times more volume than a recording site once the shank is fully inserted in the brain (Jun

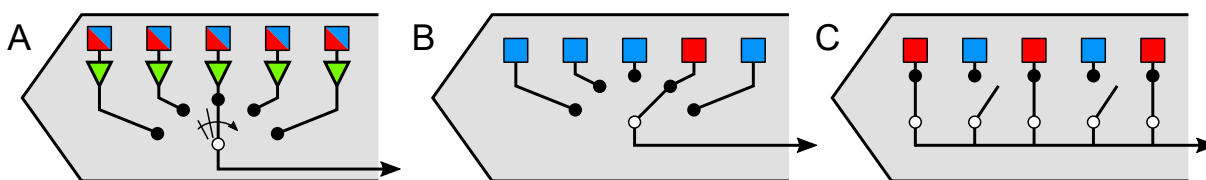


Figure 1: **Strategies for using a single wire to serve many recording sites in switchable silicon probes.** (A) Time-division multiplexing. Rapidly cycling the selector switch allows a single wire to carry signals from many recording sites interleaved in time. Triangles represent anti-aliasing filters. (B) Static switching. A single wire connects to one of many possible recording sites through a selector switch. (C) Electrode pooling. Many recording sites are connected to a single wire through multiple controllable switches.

35 [et al., 2017b](#)). The current silicon arrays invariably displace more neurons than they record, and thus the goal  
36 of “monitoring all neurons” seems unattainable by simply scaling the present approach<sup>1</sup>. Clearly we need  
37 a way to increase the number of neurons recorded while avoiding a concomitant increase in the number of  
38 wires that enter the brain.

### 39 1.1 Time-division multiplexing

40 A common approach by which a single wire can convey multiple analog signals is time-division multiplexing  
41 ([Obien et al., 2015](#)). A rapid switch cycles through the  $N$  input signals and connects each input to the output  
42 line for a brief interval (Figure 1A). At the other end of the line, a synchronized switch demultiplexes the  $N$   
43 signals again. In this way a single wire carries signals from all its associated electrodes interleaved in time.  
44 The cycling rate of the switch is constrained by the sampling theorem ([Shannon, 1949](#)): It should be at least  
45 twice the highest frequency component present in the signal. The raw voltage signals from extracellular  
46 electrodes include thermal noise that extends far into the Megahertz regime. Therefore an essential element  
47 of any such multiplexing scheme is an analog low-pass filter associated with each electrode. This anti-alias  
48 filter removes the high-frequency noise above a certain cut-off frequency. In practice the cut-off is chosen  
49 to match the bandwidth of neuronal action potentials, typically 10 kHz. Then the multiplexer switch can  
50 safely cycle at a few times that cut-off frequency.

51 Given the ubiquity of time-division multiplexing in communication electronics, what prevents its use for  
52 neural recording devices? One obstacle is the physical size of the anti-alias filter associated with each elec-  
53 trode. When implemented in CMOS technology, such a low-pass filter occupies an area much larger than the  
54 recording site itself ([Shahroghi et al., 2010](#)), which would force the electrodes apart and prevent any high-  
55 density recording<sup>2</sup>. What if one simply omitted the low-pass filter? In that case aliasing of high-frequency  
56 thermal fluctuations will increase the noise power in the recording by a factor equal to the number of elec-  
57 trodes  $N$  being multiplexed. One such device with a multiplexing factor of  $N = 128$  has indeed proven  
58 unsuitable for recording action potentials, as the noise drowns out any signal ([Eversmann et al., 2003](#)). A  
59 recent design with a more modest  $N = 8$  still produces noise power 4-15 times higher than in comparable  
60 systems without multiplexing ([Raducanu et al., 2017](#)).

61 Other issues further limit the use of time-division multiplexing: The requirement for amplification, filtering,  
62 and rapid switching right next to the recording site means that electric power gets dissipated on location,

<sup>1</sup>But see [Kleinfeld et al. \(2019\)](#) for a wildly optimistic proposal.

<sup>2</sup>One recent report claims to implement a 4 kHz low-pass filter with an electrode spacing of just 28  $\mu\text{m}$ , but the underlying circuit has never been revealed ([Angotzi et al., 2019](#)).

63 heating up exactly the neurons one wants to monitor. Furthermore, the active electronics in the local ampli-  
64 fier are sensitive to light, which can produce artifacts during bright light flashes for optogenetic stimulation  
65 (Jun et al., 2017b; Kozai and Vazquez, 2015).

## 66 1.2 Static selection

67 An alternative approach involves static electrode selection (Figure 1B). Again, there is an electronic switch  
68 that connects the wire to one of many electrodes. However the switch setting remains unchanged during  
69 the electrical recording. In this way the low-pass filtering and amplification can occur at the other end  
70 of the wire, outside the brain, where space is less constrained. The switch itself requires only minimal  
71 circuitry that fits comfortably under each recording site, even at a pitch of 20  $\mu\text{m}$  or less. Because there is  
72 no local amplification or dynamic switching, the issues of heat dissipation or photosensitivity do not arise.  
73 This method has been incorporated recently into flat electrode arrays (Müller et al., 2015) as well as silicon  
74 prongs (Jun et al., 2017b; Lopez et al., 2017; Steinmetz et al., 2021). It allows the user to choose one of many  
75 electrodes intelligently, for example because it carries a strong signal from a neuron of interest. This strategy  
76 can increase the yield of neural recordings, but it does not increase the number of neurons per wire.

## 77 1.3 Electrode pooling

78 On this background we introduce a third method of mapping electrodes to wires: select multiple electrodes  
79 with suitable signals and connect them to the same wire (Figure 1C). Instead of rapidly cycling the intervening  
80 switches, as in multiplexing, simply leave all those switches closed. This creates a "pool" of electrodes whose  
81 signals are averaged and transmitted on the same wire. At first that approach seems counterproductive,  
82 as it mixes together recordings that one would like to analyze separately. How can one ever reconstruct  
83 which neural signal came from which electrode? Existing multi-electrode systems avoid this signal mixing  
84 at all cost, often quoting the low cross-talk between channels as a figure of merit. Instead, we will show  
85 that the pooled signal can be unmixed if one controls the switch settings carefully during the recording  
86 session. Under suitable conditions this method can record many neurons per wire without appreciable loss  
87 of information.

88 We emphasize that the ideal electrode array device to implement this recording method does not yet exist.  
89 It would be entirely within reach of current fabrication capabilities, but every new silicon probe design re-  
90 quires a substantial investment and consideration of various trade-offs. With this article we hope to make  
91 the community of electrode users aware of the opportunities in this domain and start a discussion about  
92 future array designs that use intelligent electrode switching, adapted to various applications in basic and  
93 translational neuroscience.

## 94 2 Theory

### 95 2.1 Motivation for electrode pooling: spike trains are sparse in time

96 A typical neuron may fire  $\sim 10$  spikes/s on average (Attwell and Laughlin, 2001). Each action potential lasts  
97 for  $\sim 1$  ms. Therefore this neuron's signal occupies less than 1% of the time axis in an extracellular recording  
98 (e.g., see Figure 3B). Sometimes additional neurons lie close enough to the same electrode to produce large

99 spikes. That still leaves most of the time axis unused for signal transmission. Electrode pooling gives the  
100 experimenter the freedom to add more neurons to that signal by choosing other electrodes that carry large  
101 spikes. Eventually a limit will be reached when the spikes of different neurons collide and overlap in time so  
102 they can no longer be distinguished. These overlaps may be more common under conditions where neurons  
103 are synchronized to each other or to external events.

## 104 2.2 The effects of pooling on spikes and noise

105 What signal actually results when one connects two electrodes to the same wire? Figure 2A shows an  
106 idealized circuit for a hypothetical electrode array that allows electrode pooling. Here the common wire is  
107 connected via programmable switches to two recording sites. At each site  $i$ , the extracellular signal of nearby  
108 neurons reaches the shared wire through a total electrode impedance  $Z_i$ . This impedance has contributions  
109 from the metal/saline interface and the external electrolyte bath (Seidl et al., 2012; Robinson, 1968), typically  
110 amounting to  $100 \text{ k}\Omega - 1 \text{ M}\Omega$ . By comparison the CMOS switches have low impedance, typically  $\sim 100 \Omega$   
111 (Seidl et al., 2012), which we will ignore.

112 In general one must also consider the shunt impedance  $Z_S$  in parallel to the amplifier input. This can result  
113 from current leaks along the long wires as well as the internal input impedance of the amplifier. For well-  
114 designed systems, this shunt impedance should be much larger than the electrode impedances; for the  
115 Neuropixels device we will show that the ratio is at least 100. Thus one can safely ignore it for the purpose of  
116 the present approximations. In that case the circuit acts as a simple voltage divider between the impedances  
117  $Z_i$ . If a total of  $M$  electrodes are connected to the shared wire, the output voltage  $U$  is the average of the  
118 signals at the recording sites  $V_i$ , weighted inversely by the electrode impedances,

$$U = \sum_{i=1}^M c_i V_i \quad (1)$$

119 where

$$c_i = \frac{1/Z_i}{\sum_{j=1}^M 1/Z_j} \quad (2)$$

120 is defined as the pooling coefficient for electrode  $i$ . If all electrodes have the same size and surface coating,  
121 they will have the same impedance, and in that limit one expects the simple relationship

$$U = \frac{1}{M} \sum_{i=1}^M V_i. \quad (3)$$

122 Thus an action potential that appears on only one of the  $M$  electrodes will be attenuated in the pooled  
123 signal by a factor  $\frac{1}{M}$ .

124 In order to understand the trade-offs of this method, we must similarly account for the pooling of noise  
125 (Figure 2A). There are three relevant sources of noise: (1) thermal ("Johnson") noise from the impedance  
126 of the electrode; (2) biological noise ("hash") from many distant neurons whose signals are too small to

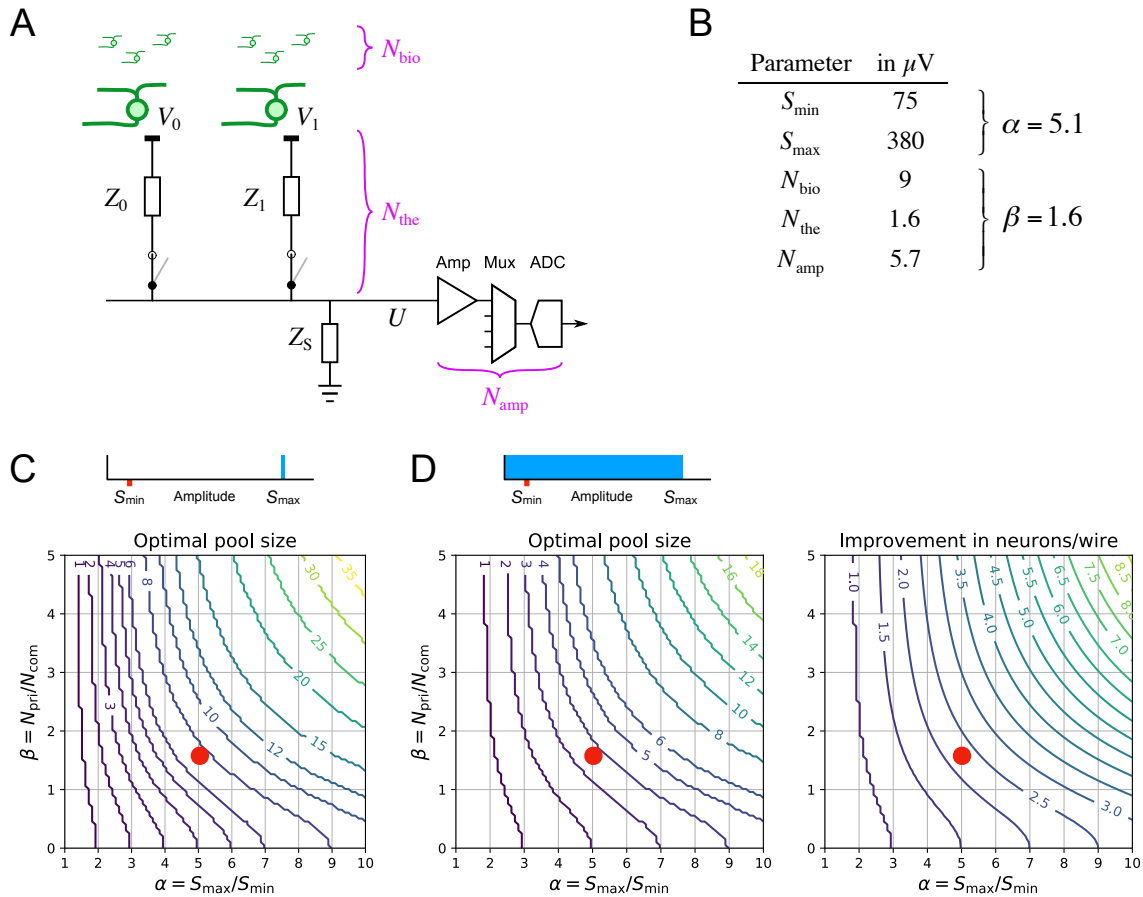


**Figure 2: Pooling of signal and noise.** (A) An idealized circuit for two electrodes connected to a common wire along with downstream components of the signal chain, such as the amplifier, multiplexer, and digitizer.  $Z_0$ ,  $Z_1$ : total impedance for electrodes 0 and 1, with contributions from the metal/bath interface and the external bath.  $Z_S$ : shunt impedance at the amplifier input. Noise sources include biological noise from distant neurons ( $N_{\text{bio}}$ ); thermal noise from the electrode impedance ( $N_{\text{the}}$ ), and common electronic noise from the amplifier and downstream components ( $N_{\text{amp}}$ ). (B) Numerical values of the relevant parameters, derived from experiments or the literature (sections 3 and 4). (C, D) The optimal electrode pool under different assumptions about the spike amplitude distribution (top insets). The contour plots show the optimal pool size and the enhancement of the neuron/wire ratio as a function of the parameters  $\alpha$  – the ratio of largest to smallest sortable spike signals – and  $\beta$  – the ratio of private to common noise. (C) Most favorable condition: Each electrode carries a single large spike of amplitude  $S_{\max}$ , and spikes are sortable down to amplitude  $S_{\min}$ . In this case the neurons/wire ratio is equal to the pool size. (D) Generic condition: Each electrode carries a uniform distribution of spike amplitudes between 0 and  $S_{\max}$ . Red dots: Conditions of  $\alpha$  and  $\beta$  encountered experimentally, based on the values in panel B.

127 be resolved; (3) electronic noise resulting from the downstream acquisition system, including amplifier,  
 128 multiplexer, and analog-to-digital converter. The thermal noise is private to each electrode, in the sense  
 129 that it is statistically independent of the noise at another electrode. The biological noise is similar across  
 130 neighboring electrodes that observe the same distant populations (Harris et al., 2000). For widely separated  
 131 electrodes the hash will be independent and thus private to each electrode, although details depend on the  
 132 neuronal geometries and the degree of synchronization of distant neurons (Schomburg et al., 2012). In that  
 133 case the private noise

$$N_{\text{pri},i} = \sqrt{N_{\text{the},i}^2 + N_{\text{bio},i}^2}. \quad (4)$$

134 because thermal noise and biological noise are additive and statistically independent.

135 Finally the noise introduced by the amplifier and data acquisition is common to all the electrodes that share  
 136 the same wire,

$$N_{\text{com}} = N_{\text{amp}}. \quad (5)$$

137 In the course of pooling, the private noise gets attenuated by the pooling coefficient  $c_i$  (Eq 2) and summed  
 138 with contributions from other electrodes. Then the pooled private noise gets added to the common noise  
 139 from data acquisition, which again is statistically independent of the other noise sources. With these as-  
 140 sumptions the total noise at the output has RMS amplitude

$$N_{\text{tot}} = \sqrt{N_{\text{com}}^2 + \sum_{i=1}^M c_i^2 N_{\text{pri},i}^2}. \quad (6)$$

141 If all electrodes have similar noise properties and impedances this simplifies to

$$N_{\text{tot}} = \sqrt{N_{\text{com}}^2 + N_{\text{pri}}^2/M}. \quad (7)$$

### 142 2.3 Theoretical benefits of pooling

143 Now we are in a position to estimate the benefits from electrode pooling. Suppose that the electrode array  
 144 records neurons with a range of spike amplitudes: from the largest, with spike amplitude  $S_{\text{max}}$ , to the  
 145 smallest that can still be sorted reliably from the noise, with amplitude  $S_{\text{min}}$ . To create the most favorable  
 146 conditions for pooling one would select electrodes that each carry a single neuron, with spike amplitude  
 147  $\sim S_{\text{max}}$  (Figure 2C). As one adds more of these electrodes to the pool, there comes a point when the  
 148 pooled signal is so attenuated that the spikes are no longer sortable from the noise. Pooling is beneficial  
 149 as long as the signal-to-noise ratio of spikes in the pooled signal is larger than that of the smallest sortable  
 150 spikes in a single-site recording, namely

$$\frac{S_{\text{max}}/M}{\sqrt{N_{\text{com}}^2 + N_{\text{pri}}^2/M}} > \frac{S_{\text{min}}}{\sqrt{N_{\text{com}}^2 + N_{\text{pri}}^2}}. \quad (8)$$

151 This leads to a limit on the pool size  $M$ ,

$$M < M_{\max} = \sqrt{\left(\frac{\beta^2}{2}\right)^2 + (1 + \beta^2)\alpha^2} - \frac{\beta^2}{2} \quad (9)$$

152 where

$$\alpha = S_{\max}/S_{\min}, \beta = N_{\text{pri}}/N_{\text{com}} \quad (10)$$

153 If one pools more than  $M_{\max}$  electrodes all the neurons drop below the threshold for sorting. So the optimal  
154 pool size  $M_{\max}$  is also the largest achievable number of neurons per wire. This number depends on two  
155 parameters: the ratio of private to common noise, and the ratio of largest to smallest useful spike amplitudes  
156 (Eq 10). These parameters vary across applications, because they depend on the target brain area, the  
157 recording hardware, and the spike-sorting software. In general, users can estimate the parameters  $\alpha$  and  $\beta$   
158 from their own experience with conventional recordings, and find  $M_{\max}$  from the graph in Figure 2C.

159 Next we consider a more generic situation, in which each electrode carries a range of spikes from different  
160 neurons (Figure 2D). For simplicity we assume a uniform distribution of spike amplitudes between 0 and  
161  $S_{\max}$ . As more electrodes are added to the pool, all the spikes are attenuated, so the smallest action poten-  
162 tials drop below the sortable threshold  $S_{\min}$ . Beyond a certain optimal pool size, more spikes are lost in the  
163 noise than are added at the top of the distribution and the total number of neurons decreases. By the same  
164 arguments used above one finds that the improvement in the number of sortable neurons,  $n_M$ , relative to  
165 conventional split recording,  $n_1$ , is

$$\frac{n_M}{n_1} = \frac{M \left( \alpha - M \sqrt{\frac{1+\beta^2/M}{1+\beta^2}} \right)}{\alpha - 1} \quad (11)$$

166 The optimal pool size  $M_{\max}$  is the  $M$  which maximizes that factor. The results are plotted in Figure 2D.

167 The benefits of pooling are quite substantial if the user can select electrodes that carry large spikes. For  
168 example under conditions of  $\alpha$  and  $\beta$  that we have encountered in practice, Figure 2C predicts that one can  
169 pool 8 electrodes and still resolve all the signals, thus increasing the neuron/wire ratio by a factor of 8. On  
170 the other extreme – with a uniform distribution of spike amplitudes – the optimal pool of 4 electrodes in-  
171 creases the neuron/wire ratio by a more modest but still respectable factor of 2.3 compared to conventional  
172 recording. The following section explains how one can maximize that yield.

## 173 2.4 Acquisition and analysis of pooled recordings

174 With these insights about the constraints posed by signal and noise one can propose an overall workflow for  
175 experiments using electrode pooling (Figure 3A). A key requirement is that the experimenter can control the  
176 switches that map electrodes to wires. This map should be adjusted to the unpredictable contingencies of  
177 any particular neural recording experiment. In fact the experimenter will benefit from using different switch  
178 settings during the same session.

179 A recording session begins with a short period of acquisition in "split mode" with only one electrode per  
180 wire. The purpose is to acquire samples of the spike waveforms from all neurons that might be recorded by

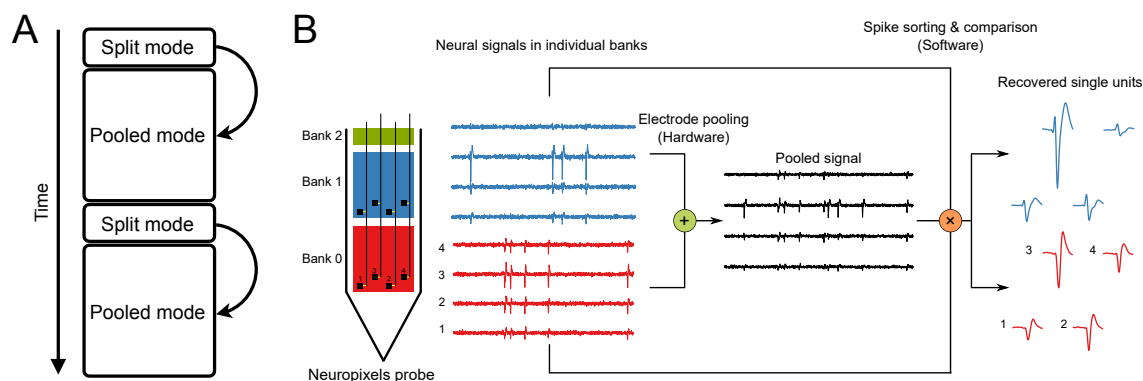


Figure 3: Workflow proposed for electrode pooling. (A) Time line of an experiment, alternating short split and long pooled recording sessions. (B) Electrode pooling using the Neuropixels probe. Recording sites (black squares, numbered from 1 to 4) in the same relative location of each bank can be pooled to a single wire by closing the switches (yellow). This generates the pooled signal (black), which is a weighted average of the signals detected in each bank (red and blue traces). From the pooled signal one recovers distinct spike shapes by spike-sorting. A comparison to the spike shapes observed in split-mode recordings allows the correct allocation of each spike to the electrodes of origin.

181 the entire array. If the device has  $E$  electrodes and  $W$  wires, this sampling stage will require  $E/W$  segments  
 182 of recording to cover all electrodes. For each segment the switches are reset to select a different batch of  
 183 electrodes. Each batch should cover a local group of electrodes, ensuring that the entire "footprint" of each  
 184 neuron can be captured.

185 During this sampling stage the experimenter performs a quick analysis to extract the relevant data that will  
 186 inform the pooling process. In particular this yields a catalog of single neurons that can be extracted by  
 187 spike-sorting. For each of those neurons one has the spike waveform observed on each electrode. Finally,  
 188 for every electrode one measures the total noise. The amplifier noise  $N_{\text{amp}}$  and thermal noise  $N_{\text{the}}$  can be  
 189 assessed ahead of time, because they are a property of the recording system, and from them one obtains  
 190 the biological noise  $N_{\text{bio}}$ . Now the experimenter has all the information needed to form useful electrode  
 191 pools. Some principles one should consider in this process:

- 192 1. Pool electrodes that carry large signals. Electrodes with smaller signals can contribute to smaller  
 193 pools.
- 194 2. Pool electrodes with distinct spike waveforms.
- 195 3. Pool distant electrodes that don't share the same hash noise.
- 196 4. Don't pool electrodes that carry dense signals with high firing rates.

197 After allocating the available wires to effective electrode pools one begins the main recording session in  
 198 pooled mode. Ideally this phase captures all neurons with spike signals that are within reach of the electrode  
 199 array.

200 In analyzing these recordings the goal is to detect spikes in the pooled signals and assign each spike cor-  
 201 rectly to its electrode of origin. This can be achieved by using the split-mode recordings from the early  
 202 sampling stage of the experiment. From the spike waveforms obtained in split-mode one can predict how  
 203 the corresponding spike appears in the pooled signals. Here it helps to know all the electrode impedances  
 204  $Z_i$  so the weighted mix can be computed accurately (Eq 1). This prediction serves as a search template for  
 205 spike-sorting the pooled recording.

206 By its very nature electrode pooling produces a dense neural signal with more instances of temporal overlap  
207 between spikes than the typical split-mode recording. This places special demands on the methods for spike  
208 detection and sorting. The conventional cluster-based algorithm (peak detection - temporal alignment - PCA  
209 - clustering) does not handle overlapping spikes well (Lewicki, 1998). It assumes that the voltage signal is  
210 sparsely populated with rare events drawn from a small number of discrete waveforms. Two spikes that  
211 overlap in time produce an unusual waveform that cannot be categorized. Recently some methods have  
212 been developed that do not force these assumptions (Yger et al., 2018; Pachitariu et al., 2016). They explicitly  
213 model the recorded signal as an additive superposition of spikes and noise. The algorithm finds an efficient  
214 model that explains the signal by estimating both the spike waveform of each neuron and its associated set  
215 of spike times. These methods are well suited to the analysis of pooled recordings.

216 Because the spike templates are obtained from split-mode recordings at the beginning of the experiment,  
217 they are less affected by noise than if one had to identify them *de novo* from the pooled recordings. Nonethe-  
218 less it probably pays to monitor the development of spike shapes during the pooled recording. If they drift  
219 too much, for example because the electrode array moves in the brain (Jun et al., 2017a), then a recalibration  
220 by another split-mode session may be in order (Figure 3A). Alternatively electrode drift may be corrected  
221 in real time if signals from neighboring electrodes are available (Steinmetz et al., 2021), a criterion that may  
222 flow into the selection of switches for pooling. Chronically implanted electrode arrays can record for months  
223 on end (Steinmetz et al., 2021), and the library of spike shapes can be updated continuously and scanned  
224 for new pooling opportunities.

225 It should be clear that the proposed workflow relies heavily on automation by dedicated software. Of course  
226 automation is already the rule with the large electrode arrays that include thousands of recording sites, and  
227 electrode pooling will require little more effort than conventional recording. Taking the newly announced  
228 Neuropixels 2.0 as a reference (5120 electrodes and 384 wires): Sampling for 5 minutes from each of the 13  
229 groups of electrodes will take a bit over an hour. Spike-sorting of those signals will proceed in parallel with  
230 the sampling and require no additional time. Then the algorithm decides on the electrode pools, and the  
231 main recording session starts. Note that these same steps also apply in conventional recording: The user  
232 still has to choose 384 electrodes among the 5120 options, and will want to scan the whole array to see  
233 where the best signals are. The algorithms we advocate to steer electrode pooling will simply become part  
234 of the software suite that runs data acquisition.

## 235 3 Experiments

### 236 3.1 Pooling characteristics of the Neuropixels 1.0 array

237 To test the biophysical assumptions underlying electrode pooling, we used the Neuropixels probe version  
238 1.0 (Jun et al., 2017b; Lopez et al., 2017). This electrode array has a single silicon shank with 960 recording  
239 sites that can be connected to 384 wires via controllable switches (Figure 3B). The electrodes are divided  
240 into three banks (called Bank 0, Bank 1, and Bank 2 from the tip to the base of the shank). In the present  
241 study only Banks 0 and 1 were used. Banks 0 and 1 each contain 383 recording sites (one channel is used  
242 for a reference signal). Each site has a dedicated switch by which it may connect to an adjacent wire. Sites  
243 at the same relative location in a bank share the same wire. These two electrodes are separated by 3.84  
244 mm along the shank. Under conventional operation of Neuropixels (Jun et al., 2017b) each wire connects to  
245 only one site at a time. However, with modifications of the firmware on the device and the user interface  
246 we engineered independent control of all the switches. This enabled a limited version of electrode pooling

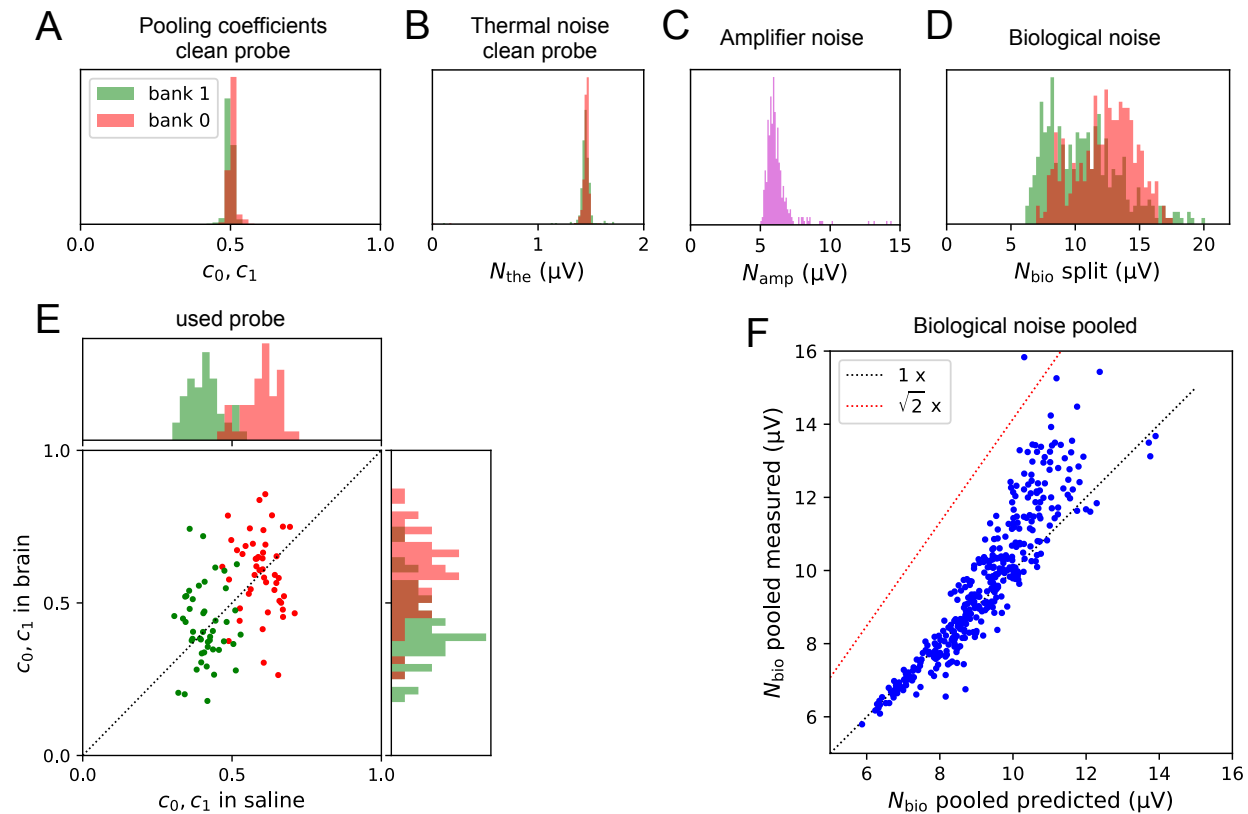


Figure 4: Pooling of signal and noise with the Neuropixels 1.0 device. (A) Pooling coefficients on a pristine probe measured in saline, histogram across all sites in banks 0 (red) and 1 (green). (B) Thermal noise (RMS) during split recording in standard saline, histogram across all sites in banks 0 and 1. (C) Amplifier noise (RMS), histogram across all 383 wires. (D) Biological noise (RMS) during brain recordings, histogram across all sites in banks 0 and 1. (E) Pooling coefficients on a used probe, measured in saline (horizontal) vs in brain (vertical). 47 pairs of sites in banks 0 and 1 with suitable action potentials. (F) Biological noise in a pooled recording measured in brain (vertical) vs the prediction derived from assuming uncorrelated noise at the two sites. '1 x': identity. ' $\sqrt{2}$  x': expectation for perfectly correlated noise.

247 across Banks 0 and 1.

248 We set out to measure those electronic properties of the device that affect the efficacy of pooling, specifically the split of the noise signal into common amplifier noise  $N_{\text{amp}}$  (Eq 7) and private thermal noise  $N_{\text{the}}$  (Eq 4), as well as the pooling coefficients  $c_i$  (Eq 2). These parameters are not important for conventional recording, and thus are not quoted in the Neuropixels user manual, but they can be derived from measurements performed in a saline bath, as described in Section 6.2.

253 On a pristine unused probe, the pooling coefficients  $c_0$  and  $c_1$  for almost all sites were close to 0.5 (Figure 254 4A), as expected from the idealized circuit (Figure 2A) if the electrode impedances are all equal (Eq 2). Correspondingly the thermal noise was almost identical on all electrodes, with an RMS value of  $1.45 \pm 0.10 \mu\text{V}$  (Fig 4B). The amplifier noise  $N_{\text{amp}}$  exceeded the thermal noise substantially, amounting to  $5.7 \mu\text{V}$  RMS on average, and more than  $12 \mu\text{V}$  for a few of the wires (Figure 4C). Because this noise source is shared across electrodes on the same wire, it lowers  $\beta$  in Equation 9 and can significantly affect electrode pooling.

## 259 3.2 Neural recording

260 Based on this electronic characterization of the Neuropixels probe we proceeded to test electrode pooling *in vivo*. Recall that each bank of electrodes extends over 3.84 mm of the shank, and one needs to implant more than one bank into the brain to accomplish any electrode pooling. Clearly the opportunities for pooling on this device are limited; nonetheless it serves as a useful testing ground for the method.

264 In the pilot experiment analyzed here, the probe was inserted into the brain of a head-fixed, awake mouse to a depth of approximately 6 mm. This involved all of Bank 0 and roughly half of Bank 1, and covered numerous brain areas from the medial preoptic area at the bottom to retrosplenial cortex at the top. Following the work flow proposed in Figure 3, we then recorded for  $\sim 10$  min each from Bank 0 and Bank 1 in split mode, followed by  $\sim 10$  min of recording from both banks simultaneously in pooled mode.

## 269 3.3 Unmixing a pooled recording

270 As proposed above, one can unmix the pooled recording by matching its action potentials to the spike waveforms sampled separately on each of the two banks (Figure 3B). Each of the three recordings (split Bank 0, split Bank 1, and pooled Banks 0 + 1) was spike-sorted to isolate single units. Then we paired each split-mode unit with the pooled-mode unit that had the most similar waveform, based on the cosine similarity of their waveform vectors (Eq 13, Figure 5B). In most cases the match was unambiguous even when multiple units were present in the two banks with similar electrode footprints (Figure 5A). The matching algorithm proceeded iteratively until the similarity score for the best match dropped below 0.9 (Figure 5B). We corroborated the resulting matches by comparing other statistics of the identified units, such as the mean firing rate and inter-spike-interval distribution (Figure 5A).

279 When spike-sorting the pooled-mode recording there is of course a strong expectation for what the spike waveforms will be, namely a scaled version of spikes from the two split-mode recordings. This suggests that one might jump-start the sorting of the pooled signal by building in the prior knowledge from sorting the split-mode recordings. Any such regularization could be beneficial, not only to accelerate the process but to compensate for the lower SNR in the pooled signal. We explored this possibility by running the template-matching function of KiloSort2 on the pooled-mode recording with templates from split-mode recordings ("hot sorting"). Then we compared this new method to two other procedures (Figure 5C): (1)

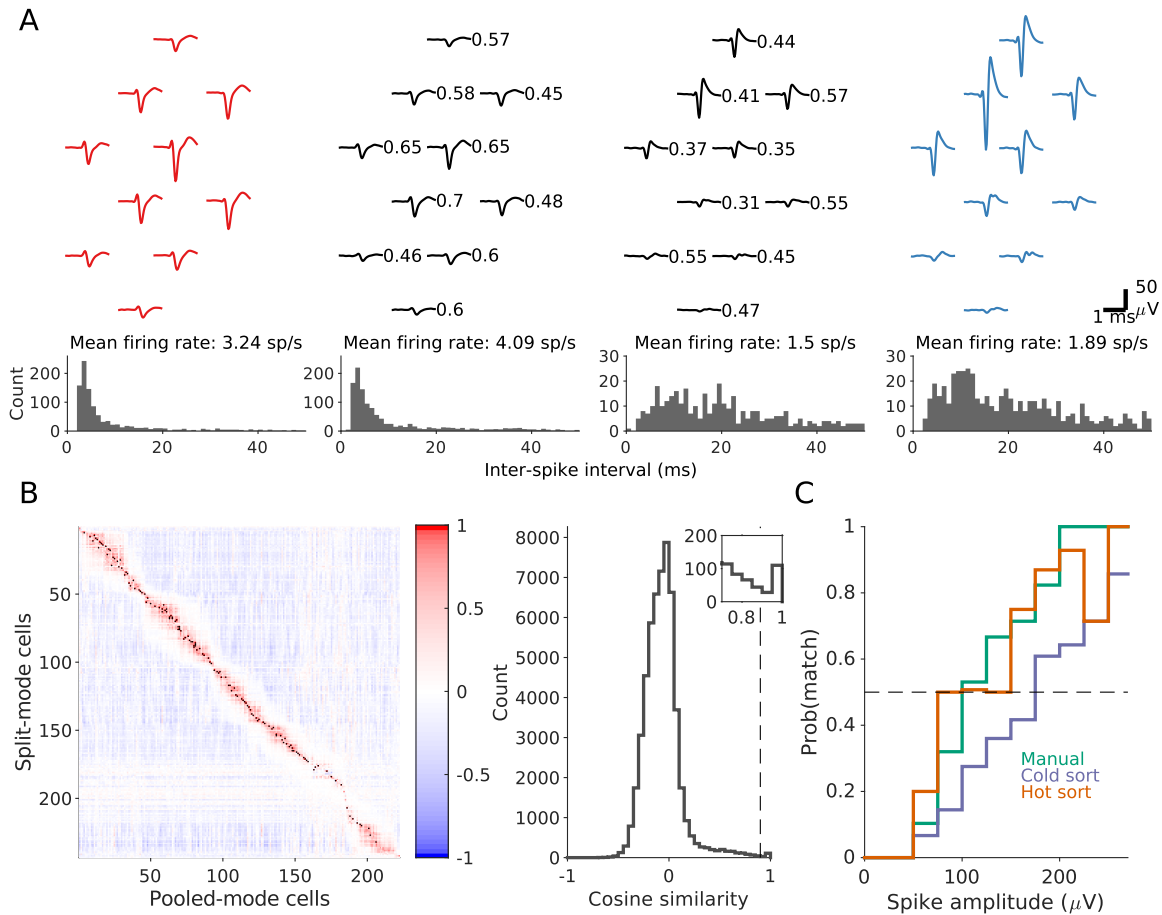


Figure 5: Recordings from mouse brain. (A) Matching spike shapes from split- and pooled-mode recordings. Top: Waveforms of two sample units (middle, black) detected in pooled mode on the same set of wires. The left unit was matched to a unit recorded in split mode from Bank 0 (red) and the right unit to one from Bank 1 (blue). Numbers indicate the scaling of the signal of the pooled-mode unit relative to its split-mode signal. Bottom: the mean firing rates and the interspike-interval distributions are similar for the matched pairs. (B) Left: matrix of the cosine similarity between units recorded in pooled- and split-mode, arranged by depth. Black dot indicates greater than the threshold at 0.9. Right: distribution of the cosine similarity. Dashed line indicates threshold at 0.9. Inset zooms into the 0.7-1 range of the distribution. (C) Probability of a unit from split recording to be matched to a unit in the pooled recording as a function of spike amplitude. Three different sorting conditions are shown: sorting all recordings by KiloSort1 followed by manual curation (Manual), sorting all recordings by KiloSort2 (Cold sort), and sorting the pooled recording by KiloSort2 with templates initialized from the split recordings (Hot sort). Dashed line indicates 50% matching probability, or the yield "break-even" point.

286 sorting each recording separately, using KiloSort1 with manual curation ("manual") and (2) sorting each  
287 recording separately using KiloSort2 with no manual intervention ("cold sorting").

288 Figure 5C illustrates what fraction of the units identified in the two split mode recordings were recovered  
289 from the pooled recording, and how that fraction depends on the spike amplitude. First, this shows that  
290 hot sorting significantly outperforms cold sorting, and in fact rivals the performance of manually curated  
291 spike sorting. This is important, because manual sorting by a human operator will be unrealistic for the  
292 high-count electrode arrays in which electrode pooling may be applied. Second, one sees that the fraction of  
293 spikes recovered exceeds 0.5 even at moderate spike amplitudes of 100  $\mu$ V. For spikes of that amplitude and  
294 above the pooled recording will contain more neurons than the average split recording. Clearly, electrode  
295 pooling is not restricted to the largest spikes in the distribution, but can be considered for moderate spike  
296 amplitudes as well.

297 Recall that the Neuropixels 1.0 probe is not optimized for electrode pooling, in that it has a fixed switching  
298 matrix, and only 2 banks of electrodes fit in the mouse brain. Thus our pilot experiments were limited to  
299 brute-force pooling the two banks site-for-site without regard to the design principles for electrode pools  
300 (Section 2.4). Nonetheless the "hot sorting" method recovered more neurons from the pooled recording  
301 (184) than on average over the two split recordings (166). We conservatively focused this assessment only on  
302 units identified in the split recordings, ignoring any unmatched units that appeared in the pooled recording.  
303 This validates the basic premise of electrode pooling even under the highly constrained conditions. Overall,  
304 the above sequence of operations demonstrates that a pooled-mode recording can be productively unmixed  
305 into the constituent signals, and the resulting units assigned to their locations along the multi-electrode  
306 shank.

### 307 3.4 Pooling of signal and noise *in vivo*

308 Closer analysis of the spike waveforms from split and pooled recordings allowed an assessment of the pool-  
309 ing coefficients *in vivo*. When spikes are present on the corresponding electrodes in both banks (as in Fig  
310 5A) one can measure the pooling coefficients  $c_0$  and  $c_1$  of Eq 2. Unexpectedly, instead of clustering near 0.5,  
311 these pooling coefficients varied over a wide range (Figure 4E), at least by a factor of 3. The two banks had  
312 systematically different pooling coefficients, suggesting that the impedance was lower for electrodes near  
313 the tip of the array.

314 Following this *in vivo* recording we cleaned the electrode array by the recommended protocol (tergazyme /  
315 water) and then measured the pooling coefficients in saline. Again the pooling coefficients varied consider-  
316 ably across electrodes, although somewhat less than observed *in vivo* (Figure 4E). Also the bath resistance  
317 of the electrodes was larger on average than on an unused probe (30 k $\Omega$  as opposed to 13 k $\Omega$ ). This change  
318 may result from the interactions within brain tissue. For example some material may bind to the electrode  
319 surface and thus raise its bath resistance. This would lower the pooling coefficient of the affected elec-  
320 trode and raise that of its partners. Because the thermal noise is never limiting (Figure 4B-D), such a change  
321 would easily go unnoticed in conventional single-site recording. The precise reason for the use-dependent  
322 impedance remains to be understood.

323 To measure the contributions of biological noise *in vivo* we removed from the recorded traces all the de-  
324 tected spikes and analyzed the remaining waveforms. After subtracting (in quadrature) the known thermal  
325 and electrical noise at each site (Figure 4B,C) one obtains the biological noise  $N_{\text{bio}}$ . This noise source sub-  
326 stantially exceeded both the thermal and amplifier noise (Figure 4F). It also showed different amplitude on  
327 the two banks, presumably owing to differences between brain areas 3.84 mm apart.

328 Given this large distance between electrodes in the two banks, one expects the biological noise to be statis-  
329 tically independent between the two sites, because neurons near one electrode will be out of reach of the  
330 other. To verify this in the present recordings we measured the biological noise in the pooled condition and  
331 compared the result to the prediction from the two split recordings, assuming that the noise was private to  
332 each site. Indeed the noise in the pooled signal was largely consistent with the assumption of independent  
333 noise (Figure 4F). It seems likely that the 1-cm shank length on these and similar array devices suffices for  
334 finding electrodes that carry independent biological noise.

## 335 4 Simulations

336 How many electrodes could experimenters pool and still sort every neuron with high accuracy? In Section  
337 2.3 we derived a theoretical limit to electrode pooling based solely on the signal and noise amplitudes.  
338 To explore what additional limitations might arise based on the density of spikes in time and the needs  
339 of spike sorting we performed a limited simulation of the process (Figure 6A). We simulated units with an  
340 extracellular footprint extending over 4 neighboring electrodes, and then pooled various such tetrodes into  
341 a single 4-channel recording. These pooled signals were then spike-sorted and the resulting spike trains  
342 compared to the known ground-truth spike times, applying a popular metric of accuracy (Magland et al.,  
343 2020). This revealed how many neurons can be reliably recovered depending on the degree of electrode  
344 pooling (Figure 6B). Then we evaluated the effects of various parameters of the simulation, such as the  
345 amplitude of the largest spikes, the biological noise, and the average firing rate.

346 For simplicity we focused on the favorable scenario of Figure 2C: It presumes that the experimenter can  
347 choose for pooling a set of tetrodes that each carry a single unit plus noise. The curves of recovered units  
348 vs pool size have an inverted-U shape (Figure 6B). For small electrode pools one can reliably recover all the  
349 units. Eventually, however, some of the units drop out, and for a large pool size all the recovered units fall  
350 below the desired quality threshold. We will call the pool that produces the largest number of recovered  
351 units the "optimal pool".

352 For the "standard" condition of simulations we chose a reasonably large spike amplitude of 380  $\mu\text{V}$  peak-to-  
353 peak (the 90-th percentile in a database of recordings by the Allen Institute (Siegle et al., 2019)), a firing rate  
354 of 10 Hz, and all the noise values as determined experimentally from the Neuropixels 1.0 device (Sections 3.1  
355 and 3.4). Under these conditions one can pool up to 5 electrodes per wire and still recover all 5 of the units  
356 reliably (Figure 6B). This optimal pool size is sensitive to the amplitude of the spikes: If the spike amplitude  
357 is reduced by a factor of 2, the optimal pool drops from 5 to 3 electrodes. Similarly, if the biological noise  
358 increases to 15  $\mu\text{V}$ , the optimal pool is reduced to 4 electrodes. This indicates that the recovery of the  
359 units from the pooled signal is strongly determined by the available signal-to-noise ratio at each electrode.  
360 By contrast increasing the firing rate two-fold to 20 Hz did not change the optimal pool from 5. Thus the  
361 temporal overlap of spikes is not yet a serious constraint. Looking to the future, if the amplifier noise on each  
362 wire could be reduced by a factor of 2 the optimal pool would expand significantly from 5 to 7 electrodes or  
363 more (Figure 6B).

364 How do these practical results relate to theoretical bounds we derived in Section 2.3? Recall that this bound  
365 depends on the noise properties, but also on the ratio of largest to smallest sortable spikes. In our "standard"  
366 simulation with a pool size of 1 (split mode) we found that the smallest sortable spikes had an amplitude of  
367 75  $\mu\text{V}$ . This also corresponds to the low end of sorted spikes reported by the Allen Institute (10-th percentile  
368 (Siegle et al., 2019)). With these bounds on large and small spikes, and the measured values of private and  
369 common noise, one obtains  $\alpha = 5.1$  and  $\beta = 1.6$  in Equation 9, which predicts an optimal pool of  $M_{\max} = 8$

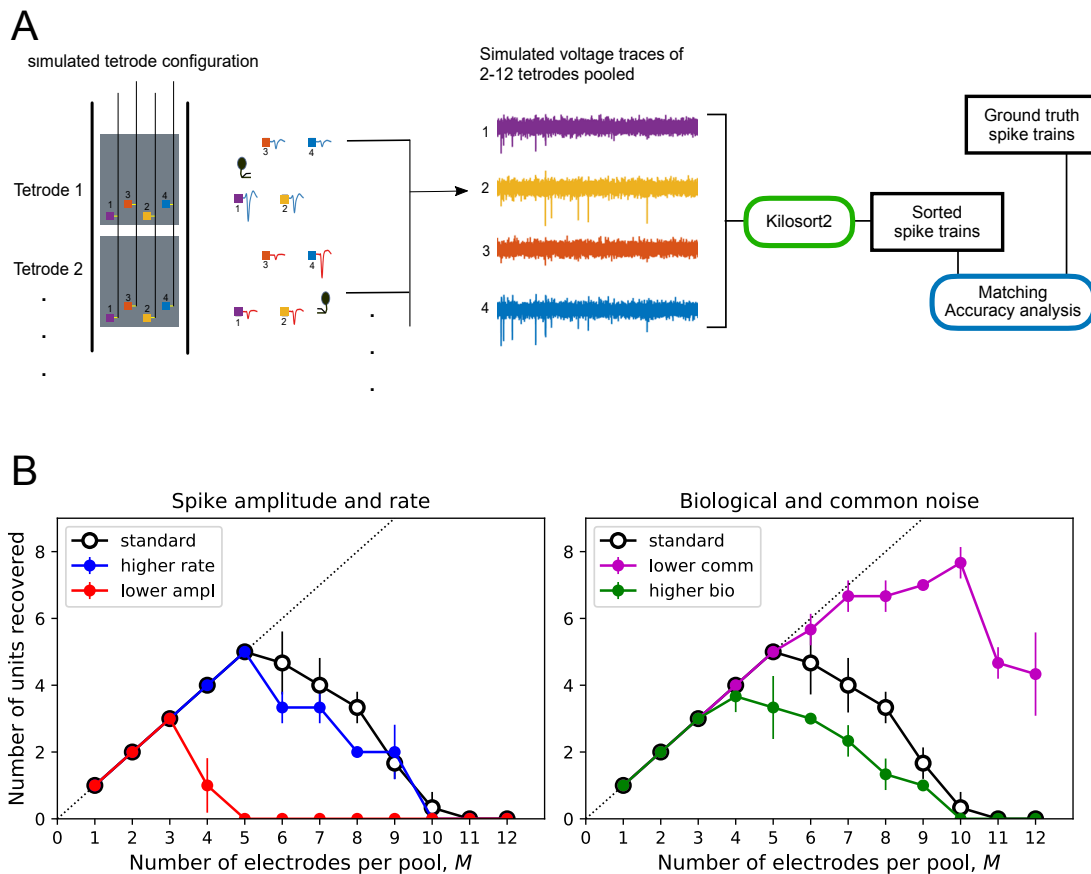


Figure 6: Simulations of electrode pooling. (A) Workflow: Groups of 4 recording sites ("tetrodes") each carry a spike train from one simulated unit, superposed with electrode noise and biological noise. Between  $M = 1$  and 12 of these tetrodes are then pooled into a single 4-wire recording followed by addition of common noise. The pooled signal is sorted and the resulting single-unit spike trains are matched with the ground truth spike trains from the  $M$  tetrodes. Units with an accuracy metric  $> 0.8$  are counted as recovered successfully. (B) Number of units recovered as a function of the pool size,  $M$ , under various conditions of simulation. Effects of varying different parameters. The "standard" condition serves as a reference: Spike amplitude  $V = 380 \mu\text{V}$ , spike rate  $r = 10 \text{ Hz}$ , electrode noise  $N_{\text{ele}} = 1.6 \mu\text{V}$ , common noise  $N_{\text{com}} = 5.7 \mu\text{V}$ , biological noise  $N_{\text{bio}} = 9 \mu\text{V}$ . "lower ampl":  $V = 205 \mu\text{V}$ . "higher rate":  $r = 20 \text{ Hz}$ . "higher bio":  $N_{\text{bio}} = 15 \mu\text{V}$ . "lower com":  $N_{\text{com}} = 2.85 \mu\text{V}$ . Each parameter combination was simulated 3 times with noise and spike times resampled, error bars are SD.

370 (Fig 2C), compared to the actually observed value of 5. The simple theory based purely on signal and noise  
 371 amplitude gives a useful estimate, but additional practical constraints that arise from temporal processing  
 372 and spike-sorting lower the yield somewhat from there.

373 In summary, under favorable conditions where the experimenter can select electrodes, the pooling method  
 374 may increase the number of units recorded per wire by a factor of 5. Even for significantly smaller spikes or  
 375 higher biological noise one can expect a factor of 3. And with future technical improvements a factor of 7  
 376 or more is plausible.

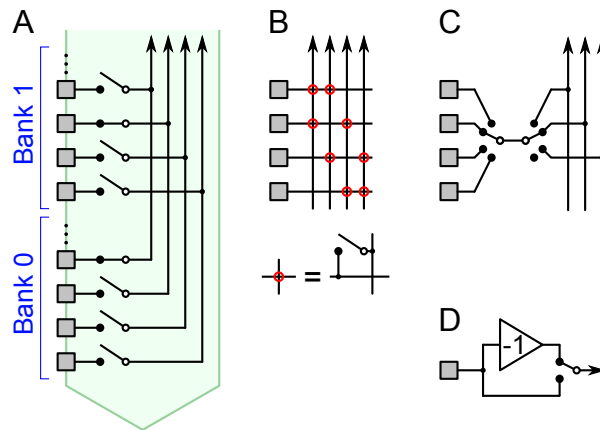


Figure 7: Hardware schemes for flexible connection between electrodes and wires. (A) In the current Neuropixels array each electrode can be connected to just one wire with a controllable switch. (B) Two switches per electrode would allow a choice of 2 wires, enabling many more pooling configurations. (C) Because neighboring electrodes often carry redundant signals, one may want to choose just one from every group of 4. This switch circuit matches that choice with one of 3 (or no) wires. (D) An optional inverter for each electrode, controlled by a local switch.

## 377 5 Discussion

### 378 5.1 Summary of results

379 This work presents the concept of electrode pooling as a way to multiply the yield of large electrode ar-  
380 rays. We show how the signals from many recording sites can be combined onto a small number of wires,  
381 and then recovered by a combination of experimental strategy and spike-sorting software. The reduced re-  
382 quirement for wires coursing through the brain will lead to slender array devices that cause less damage to  
383 the neurons they are meant to observe. We developed the theory behind electrode pooling, analyzed the  
384 trade-offs of the approach, derived a mathematical limit to pooling, and developed a recipe for experiment  
385 and analysis that implements the procedure (Section 2). We also verified the basic assumptions about signal  
386 mixing and unmixing using a real existing device: the Neuropixels 1.0 probe (Section 3). We showed that  
387 signals from different neurons can be reliably disambiguated and assigned back to the electrodes of origin.  
388 For the optimal design of electrode pools and to analyze the resulting data, it is advantageous to gather  
389 precise information about impedance and noise properties of the device. In simulations we showed that  
390 with a proper selection of electrodes based on the signals they carry, the method could improve the yield  
391 of neurons per wire by a factor of 3 to 7 (Section 4).

392 Electrode pooling is categorically different from most data compression schemes that have been proposed  
393 for neural recording systems (Linderman et al., 2008; Olsson and Wise, 2005; Suo et al., 2014). In many of  
394 those applications the goal is to reduce the bit rate for data transmission out of the brain, for example using  
395 a wireless link. By contrast electrode pooling seeks to minimize the number of electrode wires one needs  
396 to stick into the brain to sample the neural signals, thus minimizing biological damage to the system under  
397 study. By itself, that doesn't reduce the bit rate, although it produces denser time series. For the optimal  
398 wireless recording system, both objectives – lower wire volume at the input and lower data volume at the  
399 output – should be combined, and their implementations are fully independent.

## 400 5.2 Future developments

### 401 5.2.1 Hardware

402 The ability to service multiple recording sites with a single wire opens the door for much larger electrode  
403 arrays that nevertheless maintain a slim form factor and don't require any onboard signal processing. On  
404 the commercially available Neuropixels 1.0 device (Jun et al., 2017b) the ratio of electrodes to wires is only  
405 2.5, and thus there is little practical benefit to be gained from electrode pooling. In most circumstances the  
406 user can probably use static selection to pick 40% of the electrodes and still monitor every possible neuron.  
407 By contrast, the recently announced Neuropixels 2.0 (Steinmetz et al., 2021) has an electrode:wire ratio  
408 of 13.3. Another device, currently in engineering test, will have 4416 sites on a single 45 mm shank, with  
409 electrode:wire ratio of 11.5. For the Neuropixels technology, the number of sites can grow with shank count  
410 and shank length while channel count is limited by base area and trace crowding on the shank. These new  
411 probes already offer substantial opportunities to pool electrodes. Indeed Steinmetz et al. (2021) report an  
412 example of pooling two electrode banks, although their approach to unmixing the signals differs from that  
413 advocated here.

414 The design of effective electrode pools requires some flexibility in how recording sites are connected to  
415 wires. In the current Neuropixels technology each electrode has only one associated wire, which constrains  
416 the choice of electrode pools. The CMOS switch itself is small, but the local memory to store the switch state  
417 occupies some silicon space (Seidl et al., 2011). Nonetheless one can implement 3 switches per electrode  
418 even on a very tight pitch (Dragas et al., 2017). When arranged in a hierarchical network (Müller et al.,  
419 2015) these switches could effect a rich diversity of pooling schemes adapted to the specifics of any given  
420 experiment (Figure 7). For example, one could route any one electrode among a group of four to any one  
421 of three wires with two 1:4 switches (Figure 7C). This requires just 1 bit of storage per electrode, as in the  
422 current Neuropixels probe (Jun et al., 2017b).

423 Another hardware design feature could greatly increase the capacity for electrode pooling: An optional  
424 analog inverter at each electrode (Figure 7D). This is a simple CMOS circuit that changes the sign of the  
425 waveform (Bae, 2019) depending on a local switch setting. If half of the electrodes in a pool use the inverter,  
426 that helps to differentiate the spike shapes of different neurons. Because extracellular signals from cell  
427 bodies generally start with a negative voltage swing, this effectively doubles the space of waveforms that  
428 occur in the pooled signal. In turn this would aid the spike-sorting analysis, ultimately allowing even more  
429 electrodes to share the same wire.

430 Of course each of these proposals comes with some cost, such as greater power use or added space required  
431 for digital logic. The overall design of a probe must take all these trade-offs into account. The several-  
432 fold gain in recording efficiency promised by electrode pooling should act as a driver in favor of fully pro-  
433 grammable switches, but deciding on the optimal design will benefit from close interaction between users  
434 and manufacturers.

### 435 5.2.2 Software

436 Electrode pooling will also benefit from further developments in spike-sorting algorithms. For example, as  
437 we discuss in Section 3.3, a promising strategy is to acquire all the spike shapes present on the electrode array  
438 using split-mode recordings, compute the expected pooled-mode waveforms, and use those as templates  
439 in sorting the pooled signals. We have implemented this so-called "hot sorting" method in KiloSort2 and

440 have shown that it can greatly increase the number of split-mode cells recovered in the pooled recordings  
441 (Figure 5C). This idea may also be extended to cluster-based sorting algorithms, by guiding the initialization  
442 of the clustering step. Indeed, knowing ahead of time which waveforms to look for in the recording would  
443 help any spike-sorter. We expect this method will also improve resolution of temporally overlapping spike  
444 waveforms.

445 As one envisions experiments with 10,000 or more recording sites, it becomes imperative to automate the  
446 optimal design of electrode pools, so that the user wastes no time before launching into pooled recording.  
447 In Section 2.4 we lay out some heuristic rules one might follow. The pooling strategy can be adapted flexibly  
448 to the statistics of the available neural signals, even varying along the silicon shank if it passes through differ-  
449 ent brain areas. The user always has the option of recording select sites in conventional mode; for example  
450 this might serve to sample local field potentials at a sparse set of locations. Designing an effective algo-  
451 rithm that recommends and implements the electrode switching based on user goals will be an interesting  
452 challenge.

### 453 **5.3 High-impact applications**

454 Finally, we believe that the flexible pooling strategy will be particularly attractive in chronic studies, where  
455 an electrode array remains implanted for months or years. In these situations, maintaining an updated  
456 library of signal waveforms is an intrinsic part of any recording strategy. Round-the-clock recording serves  
457 to populate and refine the library, enabling the design of precise spike templates, and effective separation  
458 of pooled signals. The library keeps updating in response to any slow changes in recording geometry that  
459 may take place.

460 A second important application for pooling arises in the context of sub-dural implants in humans. Here  
461 the sub-dural space forces a low-profile chip with minimal volume for electronic circuitry, whereas one can  
462 envision several slender penetrating electrode shafts with thousands of recording sites. We estimate that  
463 some devices that are now plausible (no published examples yet) will have an electrode-to-channel ratio  
464 near 25. Clearly one will want to record from more than 1/25 of the available sites, and electrode pooling  
465 achieves it without increased demand on electronic circuitry.

466 In summary, while the devices to maximize pooling benefits are not yet available, they soon may be. Consid-  
467 eration of pooling options would benefit the designers and users of these devices. The advantage of pooling  
468 grows naturally as the same tissue is recorded across sessions or time. The calculations and demonstrations  
469 reported here are intended to inspire professional simulations and design of future devices for a variety of  
470 applications, including human implants.

## 471 **6 Methods and materials**

472 All analysis was performed with Matlab R2016b (Mathworks) and Python 3. All the quoted uncertainties are  
473 standard deviations.

## 474 6.1 Control of Neuropixels switching circuitry

475 The Neuropixels 1.0 probe has 960 recording sites that can be connected to 384 wires via controllable  
476 switches. The conventional mode of operation (split mode) was to connect one electrode to one wire at a  
477 time. Electrode pooling was implemented by modifying the Neuropixels API and the GUI software [SpikeGLX](#)  
478 to allow connecting up to three electrodes to each readout wire.

## 479 6.2 Neuropixels device measurements

480 To characterize signal and noise pooling on the Neuropixels 1.0 array, we immersed the probe in a saline  
481 bath containing two annular electrodes to produce an electric field gradient (Fig 8A). The electrolyte was  
482 phosphate-buffered saline (Sigma-Aldrich P4417; 1X PBS contains 0.01 M phosphate buffer, 0.0027 M potas-  
483 sium chloride and 0.137 M sodium chloride, pH 7.4, at 25 °C). We recorded from all 383 wires (recall that one  
484 wire is a reference electrode), first closing the switches in Bank 0 then in Bank 1, then in both banks (Figure  
485 3B).

486 One set of measurements simply recorded the noise with no external field applied. Then we varied the  
487 concentrations of PBS (by factors  $10^{-3}$ ,  $10^{-2}$ ,  $10^{-1}$ , 1, and 10), which modulated the conductance of the  
488 bath electrolyte in the same proportions. For each of the 15 recording conditions (5 concentrations x 3 switch  
489 settings) we measured the root-mean-square noise on each of the 383 wires. Then we set to explain these  
490  $5 \times 3 \times 383$  noise values based on the input circuitry of the Neuropixels device. After some trial-and-error  
491 we settled on the equivalent circuit in Figure 8B. It embodies the following assumptions:

- 492 • Each electrode is a resistor  $R_i$  in series with a capacitor  $C_i$ . The resistor is entirely the bath resistance,  
493 so it scales inversely with the saline concentration.
- 494 • The shunt impedance  $Z_S$  across the amplifier input is a resistor  $R_S$  in parallel with a capacitor  $C_S$ .
- 495 • The thermal noise from this R-C network and the voltage noise  $N_{\text{amp}}$  from the amplifier and acquisition  
496 system sum in quadrature.

497 With these assumptions one can compute the total noise spectrum under each condition. In brief, each  
498 resistor in Figure 8B is modeled as a white-spectrum Johnson noise source in series with a noiseless resistor  
499 (Thevenin circuit). The various Johnson noise spectra are propagated through the impedance network to  
500 the output voltage  $U$ . That power spectrum is integrated over the AP band (300-10000 Hz) to obtain the  
501 total thermal noise. After adding the amplifier noise  $N_{\text{amp}}$  in quadrature one obtains the RMS noise at the  
502 output  $U$ . This quantity is plotted in the fits of Figure 8C.

503 The result is rather insensitive to the electrode capacitance  $C_i$  because that impedance is much lower than  
504 the shunt impedance  $Z_S$ . By contrast the bath resistance ( $R_0, R_1$ ) has a large effect because one can raise  
505 it arbitrarily by lowering the saline concentration. To set the capacitor values, we therefore used the infor-  
506 mation from the Neuropixels spec sheet that the total electrode impedance at 1 kHz is 150 k $\Omega$ ,

$$C_i = \frac{1}{2\pi \cdot 1000 \text{ Hz} \cdot \sqrt{(150 \text{ k}\Omega)^2 - R_i^2}}$$

507 We also found empirically that the shunt impedance is primarily capacitive:  $R_S$  is too large to be measured  
508 properly and we set it to infinity. Thus the circuit model has only 4 scalar parameters:  $R_0, R_1, C_S, N_{\text{amp}}$ .

509 Their values were optimized numerically to fit all 15 measurements. This process was repeated for each of  
510 the 383 wires. The fits are uniformly good, see Figure 8C for examples.

511 As expected the thermal noise increases at low electrolyte concentration because the bath impedance in-  
512 creases (Figure 8C). However, the noise eventually saturates far below the level expected for the lowest  
513 saline concentration. This reveals the presence of another impedance in the circuit that acts as a shunt  
514 across the amplifier input (Fig 2A). We found that  $Z_S \approx 20 \text{ M}\Omega$  and is mostly capacitive. Because the shunt  
515 impedance far exceeds the electrode impedances ( $\sim 150 \text{ k}\Omega$  (Jun et al., 2017b)), it has only a minor effect  
516 on signal pooling, which justifies the approximations made in Section 2.

517 The measured noise voltage also saturates at high saline concentration (Fig 8C), and remains far above the  
518 level of Johnson noise expected from the bath impedance. That minimum noise level is virtually identical  
519 for the two electrodes that connect to the same wire, whether or not they are pooled, but it varies consid-  
520 erably across wires (Figure 8D). We conclude that this is the amplifier noise  $N_{\text{amp}}$  introduced by each wire's  
521 acquisition system (Figure 2A).

522 Figure 8E shows the best-fit values of the 4 circuit parameters, histogrammed across all the wires on an  
523 unused probe. Note they fall in a fairly narrow distribution. The bath impedance of the electrodes (in normal  
524 saline) is  $\sim 13 \text{ k}\Omega$ , the shunt capacitance is  $\sim 10 \text{ pF}$ , and the common noise  $N_{\text{amp}}$  has a root-mean-square  
525 amplitude of  $\sim 6 \mu\text{V}$  integrated over the AP band (300-10000 Hz).

526 These measurements were performed on both fresh and used Neuropixels devices, with similar results. On  
527 a device previously used in brain recordings the bath impedance of the electrodes was somewhat higher:  
528  $30 \text{ k}\Omega$  instead of  $13 \text{ k}\Omega$ .

529 To measure the pooling coefficients we applied an oscillating electric field (1000 Hz) along the electrode  
530 array with a pair of annular electrodes (Figure 8A). From the recorded waveform we estimated the signal  
531 amplitude by the Fourier coefficient at the stimulus frequency. Two different field gradients (called A and  
532 B) yielded two sets of measurements, each in the two split modes ( $U_{0,A}, U_{1,A}, U_{0,B}, U_{1,B}$ ) and the pooled  
533 mode ( $U_{P,A}, U_{P,B}$ ). For each of the 383 wires we estimated the pooling coefficients of its two electrodes  
534 by solving

$$\begin{bmatrix} U_{0,A} & U_{1,A} \\ U_{0,B} & U_{1,B} \end{bmatrix} \begin{bmatrix} k_0 \\ k_1 \end{bmatrix} = \begin{bmatrix} U_{P,A} \\ U_{P,B} \end{bmatrix}$$

535 These mixing coefficients  $k_0$  and  $k_1$  express the recorded amplitude  $U_P$  in terms of the recorded amplitudes  
536  $U_0$  and  $U_1$ ,

$$U_P = k_0 U_0 + k_1 U_1 \quad (12)$$

537 whereas the pooling coefficients  $c_0$  and  $c_1$  (Eq 2) are defined relative to the input voltages  $V_0$  and  $V_1$ ,  
538 namely

$$U_P = c_0 V_0 + c_1 V_1$$

539 The  $U_i$  differ from the  $V_i$  only by the ratio of electrode impedance to shunt impedance. Given the measured  
540 value of  $Z_S \approx 20 \text{ M}\Omega$  that ratio is less than 1%, a negligible discrepancy. So the measured  $k_0$  and  $k_1$  are

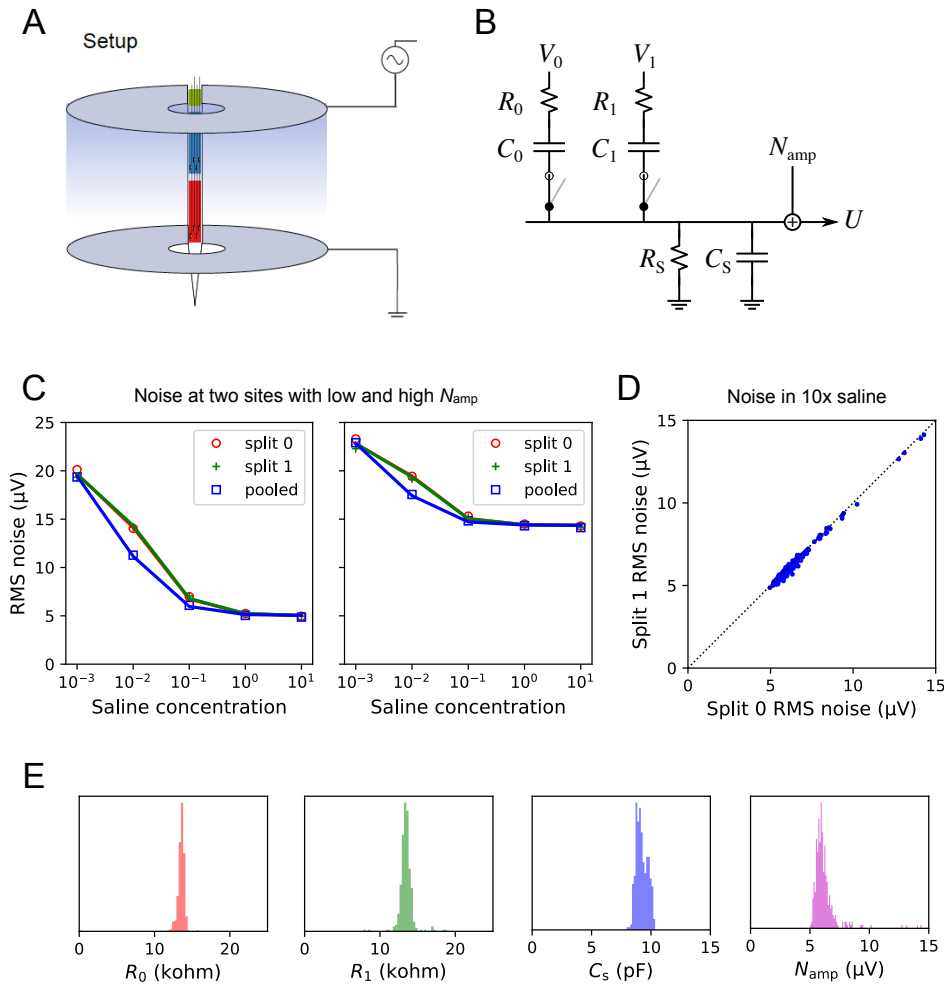


Figure 8: Methods for *in vitro* measurements of Neuropixels function. (A) The probe is immersed in saline, with two annular electrodes producing an electric gradient along the shank. (B) Equivalent circuit model to understand signal and noise pooling for one wire of the array. (C) Measurements of noise only without an external field. RMS noise as a function of the saline concentration under 3 conditions of the switches: split recording from Bank 0, split recording from Bank 1, and pooled recording from both. Examples of two different wires, one with high, the other with low amplifier noise  $N_{amp}$ . (D) The noise at the highest saline concentration, recording from electrode 1 vs electrode 0. Each dot is for one of the 383 wires. This limiting noise is identical across the two electrodes on the same wire. (E) Histograms of the best-fit circuit parameters derived for each of the 383 wires on a pristine Neuropixels probe.  $R_S$  is too large to be measured properly.

541 excellent approximations to the pooling coefficients  $c_0$  and  $c_1$ , which in turn reflect the ratio of the two  
542 electrode impedances (Eq 2).

### 543 **6.3 In vivo recording**

544 We used a Neuropixels 1.0 probe (Jun et al., 2017b) to record neural signals from a head-fixed mouse (C57BL/6J,  
545 male, 9 months old). The probe entered the brain at 400  $\mu\text{m}$  from midline and 3.7 mm posterior from bregma  
546 at  $\sim 45^\circ$  and was advanced for  $\sim 6$  mm, which corresponded to all of Bank 0 and roughly half of Bank 1. This  
547 covered many brain areas, from retrosplenial cortex at the top to medial preoptic nucleus at the bottom.  
548 Detailed description of the mouse surgery, probe implantation, and post hoc histology and imaging of probe  
549 track can be found in a previous report (Lee et al., 2020). All procedures were in accordance with institu-  
550 tional guidelines and approved by the Caltech IACUC.

551 Once the probe was implanted, data were recorded in the following order: (1) split-mode in Bank 0 (i.e. all  
552 384 wires connected to recording sites in Bank 0); (2) split-mode in Bank 1; (3) pooled-mode across Banks 0  
553 and 1. Each recording lasted for  $\sim 10$  min.

554 Following brain recordings the array was cleaned according to [recommended protocol](#) by immersion in  
555 tergazyme solution and rinsing with water.

### 556 **6.4 Spike-sorting**

557 For "manual" spike-sorting of the *in vivo* recordings we used KiloSort1 (downloaded from <https://github.com/cortex-lab/KiloSort>  
558 on Apr 10, 2018). We ran the automatic template-matching step; the detailed  
559 settings are available in the code accompanying this manuscript. This was followed by manual curation,  
560 merging units and identifying those of high quality. These manual judgements were based on requiring a  
561 plausible spike waveform with a footprint over neighboring electrodes, a stable spike amplitude, and a clean  
562 refractory period. This was done separately for each of the three recordings (split-mode Bank 0, split-mode  
563 Bank 1, pooled-mode).

564 We implemented the "hot sorting" feature in KiloSort2 (downloaded from <https://github.com/MouseLand/Kilosort2>  
565 on Mar 19, 2020). No manual curation was used in this mode, because (1) we wanted to gener-  
566 ate a reproducible outcome, and (2) manual inspection is out of the question for the high-volume recordings  
567 where electrode pooling will be applied. We first sorted the two split-mode recordings and used their tem-  
568 plates to initialize the fields  $\bar{W}$  and  $\bar{U}$  of `rez2` before running the main template-matching function on the  
569 pooled recording (see the accompanying code for more details). Finally, the splits, merges, and amplitude  
570 cutoffs in KiloSort2 ensured that the final output contained as many well-isolated units as possible. We then  
571 selected cells designated as high quality (KSLabe1 of Good) by KiloSort2, indicating putative, well-isolated  
572 single neurons (Stringer et al., 2019).

573 To elaborate on the internal operations of KiloSort2: Spike-sorted units were first checked for potential  
574 merges with all other units that had similar multi-channel waveforms (waveform correlation  $> 0.5$ ). If the  
575 cross-correlograms had a large dip ( $< 0.5$  of the stationary value of the cross-correlogram) in the range  $[-1$   
576  $\text{ms}, +1 \text{ms}]$ , then the units were merged. At the end of this process, units with at least 300 spikes were  
577 checked for refractory periods in their auto-correlograms, which is a measure of contamination with spikes  
578 from other neurons. The contamination index was defined as the fraction of refractory period violations

579 relative to the stationary value of the auto-correlogram. The default threshold in Kilosort2 of 10 percent  
580 maximum contamination was used to determine good, well-isolated units.

581 Following spike sorting, we applied the matching algorithm based on cosine similarity described in Section  
582 3.3 to determine how many cells identified in split recordings could be recovered from the pooled recording.  
583 This was compared with the results from “cold sorting,” in which the pooled recording was sorted on its own,  
584 as well as to the conventional sorting that includes manual curation (Figure 5C).

## 585 6.5 Unmixing pooled signals

586 After sorting the split and pooled recordings, we computed the average waveform of every cell. Specifically,  
587 for each cell we averaged over the first  $n$  spikes, where  $n$  was the lesser of 7500 or all the spikes the cell  
588 fired during the recording.

589 We then sought to identify every cell in the pooled recordings with a cell in the split recordings. This was  
590 done by the following procedure: Let  $S$  denote a cell sorted from the split-mode recording ( $S \in \mathcal{S}$ ) and  $S_i$   
591 its waveform at channel  $i$ . Although  $i$  can range from 1 to 384 (the total number of wires available in the  
592 Neuropixels probe), we only focus on the 20 channels above and 20 channels below the channel with the  
593 largest amplitude ( $i'$ ), i.e.  $J = [i' - 20, i' + 20]$ . We wish to find the cell  $P$  from the pooled-mode recordings  
594 ( $P \in \mathcal{P}$ ) that is closest to  $S$ . To do so, we compute the cosine similarity score for each pair ( $S, P$ ):

$$\Sigma(S, P) = \frac{\mathbf{S} \cdot \mathbf{P}}{\|\mathbf{S}\| \|\mathbf{P}\|} \quad (13)$$

595 where  $\mathbf{S}$  and  $\mathbf{P}$  are column vectors obtained by concatenating every  $S_j$  and  $P_j$  ( $j \in J$ ), respectively, and  
596  $\|\cdot\|$  is the  $\ell^2$  norm.  $\Sigma$  is a  $|\mathcal{S}|$ -by- $|\mathcal{P}|$  matrix. We identify the largest element of  $\Sigma$ , which corresponds to the  
597 most similar pair of  $S$  and  $P$ . We then update  $\Sigma$  by removing the row and column of this largest element.  
598 This process gets iterated until every  $P \in \mathcal{P}$  is given a best match. By manual inspection we found that pairs  
599 with similarity score greater than 0.9 were good matches.

## 600 6.6 Estimating pooling coefficients *in vivo*

601 Once each  $P \in \mathcal{P}$  was assigned a match  $S \in \mathcal{S}$ , the pooling coefficient ( $k_i$ ) was computed by solving the  
602 optimization problem below for each  $i$  with a least squares method (`mldivide` in Matlab).

$$\arg \min_{k_i} \|S_i - k_i P_i\| \quad (14)$$

603 Sometimes a single recording site detected action potentials from multiple cells. As a result its pooling  
604 coefficient could be estimated from the signal of each of these cells. Typically these estimates deviated  
605 from each other by less than 0.1. In these cases we assigned the average of these values as the pooling  
606 coefficient of the recording site.

607 When two recording sites that share a wire in pooled-mode each carry significant signal, it enables the  
608 estimation of both of their pooling coefficients. Examples of such sites are shown in Figures 5D-E (up to 50  
609 pairs in Banks 0 and 1).

## 610 **6.7 Simulation**

### 611 **6.7.1 Generating simulated data**

612 We simulated extracellular voltage signals on 12 groups of 4 local electrodes ("tetrodes"). Each time series  
613 was sampled at 30,000 samples/s and extended over 600 s. After combining signal and noise as described  
614 below, the time series was filtered with a passband of 300-5000 Hz.

615 Each tetrode carried spikes from a single unit. The spike waveform of the unit was chosen from an actual  
616 mouse brain Neuropixel recording, with a different waveform on each tetrode. Within a tetrode, one elec-  
617 trode chosen at random carried this spike at the nominal peak-to-peak amplitude,  $V$  (Figure 6B). On the  
618 other 3 electrodes the spike was scaled down by random factors drawn from a uniform distribution over  
619  $[0,1]$ . The spike train was simulated as a Poisson process with a forced 2-ms refractory period, having aver-  
620 age firing rate  $r$  (Figure 6B).

621 Three sources of noise - biological noise  $N_{\text{bio}}$ , thermal electrode noise  $N_{\text{the}}$ , and common amplifier noise  
622  $N_{\text{com}}$  - were generated as gaussian processes. The quoted noise values (Figure 6B) refer to root-mean-  
623 square amplitude over the 300-5000 Hz passband. Thermal noise was sampled independently for each  
624 electrode, but the biological noise was identical for electrodes within a tetrode, given that they likely observe  
625 the same background activity.

626 Electrode pooling across  $M$  tetrodes was implemented by combining the voltage signals of the correspond-  
627 ing electrode on each tetrode, resulting in signals on 4 wires. In the process each electrode signal was  
628 weighted by  $1/M$ , then the amplifier noise was added to the resulting average. Amplifier noise was sam-  
629 pled separately for each wire.

630 Tetrodes were added to the pool in a sequence determined by the spike shape of their units (see Section  
631 2.4). We started with the two most dissimilar units as determined by the cosine similarity of their spike  
632 waveforms. Then we progressively added the unit that had the lowest similarity with those already in the  
633 pool.

### 634 **6.7.2 Sorting simulated data**

635 The simulated 4-wire time series was sorted using Kilosort2; detailed configuration settings are available  
636 in the code accompanying this paper. We found it necessary to turn off the "median voltage subtraction"  
637 during preprocessing, because that feature somehow introduced artifacts in the 4 voltage traces. This did  
638 not occur when processing electrode array data with many channels, for which the algorithm is intended.  
639 We note that an effective means of subtracting the common signal across wires may help suppress the  
640 biological noise and lead to better sorting results.

641 When large numbers of tetrodes were pooled the signal-to-noise ratio dropped to the point where KiloSort2  
642 could not form templates in the preprocessing step. Under those conditions we report zero units recovered  
643 (Figure 6B).

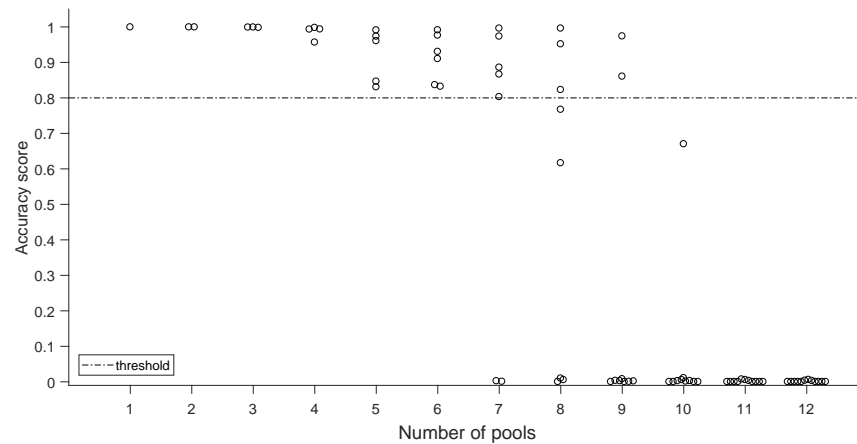


Figure 9: Accuracy scores of one "standard" condition simulation, Related to Fig 6. Units with accuracy score > 0.8 were counted as recovered.

### 644 6.7.3 Scoring simulated data

645 Following previous reports (Barnett et al., 2016; Magland et al., 2020), the spike times of the sorted units  
 646 and the ground truth units were matched and compared using the confusion matrix algorithm from Barnett  
 647 et al. (2016). We set the acceptable time error between sorted spikes and ground-truth spikes at 0.1 ms.  
 648 Then we counted the number of spike pairs with matching spike times,  $n_{\text{match}}$ , the number of unmatched  
 649 spikes in the ground-truth unit,  $n_{\text{miss}}$ , and the number of unmatched false-positive spikes in the sorted unit,  
 650  $n_{\text{fp}}$ .

651 To assess the quality of the match between ground-truth and sorted units we adopted the Accuracy defini-  
 652 tion in (Magland et al., 2020):

$$\text{Accuracy} = \frac{n_{\text{match}}}{n_{\text{match}} + n_{\text{miss}} + n_{\text{fp}}} \quad (15)$$

653 Figure 9 shows the accuracy distribution obtained for various degrees of pooling. Sorted units with accuracy  
 654 > 0.8 were counted as "recovered" from the pooled signal. For each parameter set we ran the simulation  
 655 3 times, randomizing the noise and the spike times. Results from the 3 runs are reported by mean  $\pm$  SD  
 656 (Figure 6B).

## 657 7 Acknowledgements

658 Funding: This work was supported by a grant from NINDS (5R01NS111477 to MM) and an award from the  
 659 Tianqiao and Chrissy Chen Institute for Neuroscience (to MM).

## 660 References

- 661 Angotzi, G. N., Boi, F., Lecomte, A., Miele, E., Malerba, M., Zucca, S., Casile, A., and Berdondini, L. (2019).  
662 SiNAPS: An implantable active pixel sensor CMOS-probe for simultaneous large-scale neural recordings.  
663 *Biosensors and Bioelectronics*, 126:355–364.
- 664 Attwell, D. and Laughlin, S. B. (2001). An energy budget for signaling in the grey matter of the brain. *J Cereb*  
665 *Blood Flow Metab*, 21:1133–45.
- 666 Bae, W. (2019). CMOS Inverter as Analog Circuit: An Overview. *Journal of Low Power Electronics and Appli-*  
667 *cations*, 9:26, DOI: [10.3390/jlpea9030026](https://doi.org/10.3390/jlpea9030026).
- 668 Barnett, A. H., Magland, J. F., and Greengard, L. F. (2016). Validation of neural spike sorting algorithms  
669 without ground-truth information. *Journal of Neuroscience Methods*, 264:65 – 77, ISSN: 0165-0270,  
670 DOI: <https://doi.org/10.1016/j.jneumeth.2016.02.022>, [http://www.sciencedirect.com/](http://www.sciencedirect.com/science/article/pii/S0165027016300036)  
671 [science/article/pii/S0165027016300036](http://www.sciencedirect.com/science/article/pii/S0165027016300036).
- 672 BRAIN Working Group, . (2014). BRAIN 2025: A Scientific Vision. Technical report, [https://](https://braininitiative.nih.gov/strategic-planning/brain-2025-report)  
673 [braininitiative.nih.gov/strategic-planning/brain-2025-report](https://braininitiative.nih.gov/strategic-planning/brain-2025-report).
- 674 Dimitriadis, G., Neto, J. P., Aarts, A., Alexandru, A., Ballini, M., Battaglia, F., Calcaterra, L., David, F., Fiáth, R.,  
675 Frazão, J., Geerts, J. P., Gentet, L. J., Van Helleputte, N., Holzhammer, T., van Hoof, C., Horváth, D., Lopes,  
676 G., Lopez, C. M., Maris, E., Marques-Smith, A., Márton, G., McNaughton, B. L., Meszéna, D., Mitra, S.,  
677 Musa, S., Neves, H., Nogueira, J., Orban, G. A., Pothof, F., Putzeys, J., Raducanu, B., Ruther, P., Schroeder,  
678 T., Singer, W., Tiesinga, P., Ulbert, I., Wang, S., Welkenhuysen, M., and Kampff, A. R. (2018). Why not record  
679 from every channel with a CMOS scanning probe? *bioRxiv*, DOI: [10.1101/275818](https://doi.org/10.1101/275818), [http://biorxiv.](http://biorxiv.org/lookup/doi/10.1101/275818)  
680 [org/lookup/doi/10.1101/275818](http://biorxiv.org/lookup/doi/10.1101/275818).
- 681 Dragas, J., Viswam, V., Shadmani, A., Chen, Y., Bounik, R., Stettler, A., Radivojevic, M., Geissler, S., Obien,  
682 M. E. J., Müller, J., and Hierlemann, A. (2017). In Vitro Multi-Functional Microelectrode Array Featuring  
683 59 760 Electrodes, 2048 Electrophysiology Channels, Stimulation, Impedance Measurement, and Neuro-  
684 transmitter Detection Channels. *IEEE Journal of Solid-State Circuits*, 52(6):1576–1590, ISSN: 0018–9200,  
685 DOI: [10.1109/JSSC.2017.2686580](https://doi.org/10.1109/JSSC.2017.2686580).
- 686 Eversmann, B., Jenkner, M., Hofmann, F., Paulus, C., Brederlow, R., Holzapfl, B., Fromherz, P., Merz, M.,  
687 Brenner, M., Schreiter, M., Gabl, R., Plehnert, K., Steinhauser, M., Eckstein, G., Schmitt-Landsiedel, D., and  
688 Thewes, R. (2003). A 128 x 128 cmos biosensor array for extracellular recording of neural activity. *IEEE*  
689 *Journal of Solid-State Circuits*, 38(12):2306–2317, ISSN: 0018–9200, DOI: [10.1109/JSSC.2003.819174](https://doi.org/10.1109/JSSC.2003.819174),  
690 <http://ieeexplore.ieee.org/document/1253878/>.
- 691 Harris, K. D., Henze, D. A., Csicsvari, J., Hirase, H., and Buzsaki, G. (2000). Accuracy of tetrode spike sep-  
692 aration as determined by simultaneous intracellular and extracellular measurements. *J Neurophysiol*,  
693 84:401–14.
- 694 Jun, J., Mitelut, C., Lai, C., Gratiy, S. L., Anastassiou, C. A., and Harris, T. D. (2017a). Real-time spike sorting  
695 platform for high-density extracellular probes with ground-truth validation and drift correction. *bioRxiv*,  
696 pages 1–29, DOI: <https://doi.org/10.1101/101030>.
- 697 Jun, J. J., Steinmetz, N. A., Siegle, J. H., Denman, D. J., Bauza, M., Barbarits, B., Lee, A. K., Anastassiou,  
698 C. A., Andrei, A., Aydin, [Ü+FFFD], Barbic, M., Blanche, T. J., Bonin, V., Couto, J., Dutta, B., Gratiy, S. L.,  
699 Gutnisky, D. A., Häusser, M., Karsh, B., Ledochowitsch, P., Lopez, C. M., Mitelut, C., Musa, S., Okun, M.,  
700 Pachitariu, M., Putzeys, J., Rich, P. D., Rossant, C., Sun, W. L., Svoboda, K., Carandini, M., Harris, K. D.,

- 701 Koch, C., O'Keefe, J., and Harris, T. D. (2017b). Fully integrated silicon probes for high-density recording of  
702 neural activity. *Nature*, 551(7679):232–236, ISSN: 14764687, DOI: [10.1038/nature24636](https://doi.org/10.1038/nature24636), <http://dx.doi.org/10.1038/nature24636>.  
703
- 704 Kleinfeld, D., Luan, L., Mitra, P. P., Robinson, J. T., Sarpeshkar, R., Shepard, K., Xie, C., and Harris, T. D. (2019).  
705 Can One Concurrently Record Electrical Spikes from Every Neuron in a Mammalian Brain? *Neuron*,  
706 103(6):1005–1015, ISSN: 08966273, DOI: [10.1016/j.neuron.2019.08.011](https://doi.org/10.1016/j.neuron.2019.08.011), <https://linkinghub.elsevier.com/retrieve/pii/S0896627319306956>.  
707
- 708 Kozai, T. D. Y. and Vazquez, A. L. (2015). Photoelectric artefact from optogenetics and imaging on micro-  
709 electrodes and bioelectronics: New challenges and opportunities. *Journal of Materials Chemistry B*,  
710 3(25):4965–4978, ISSN: 2050–7518, DOI: [10.1039/C5TB00108K](https://doi.org/10.1039/C5TB00108K).
- 711 Lee, K. H., Tran, A., Turan, Z., and Meister, M. (2020). The sifting of visual information in the superior  
712 colliculus. *eLife*, 9, ISSN: 2050–084X, DOI: [10.7554/eLife.50678](https://doi.org/10.7554/eLife.50678).
- 713 Lewicki, M. S. (1998). A review of methods for spike sorting: the detection and classification of neural action  
714 potentials. *Network*, 9 4:R53–78.
- 715 Linderman, M. D., Santhanam, G., Kemere, C. T., Gilja, V., O'Driscoll, S., Yu, B. M., Afshar, A., Ryu, S. I., Shenoy,  
716 K. V., and Meng, T. H. (2008). Signal processing challenges for neural prostheses. *Ieee Signal Processing  
717 Magazine*, 25(1):18–28, ISSN: 1053–5888, DOI: [10.1109/MSP.2008.4408439](https://doi.org/10.1109/MSP.2008.4408439).
- 718 Lopez, C. M., Putzeys, J., Raducanu, B. C., Ballini, M., Wang, S., Andrei, A., Rochus, V., Vandebriel, R., Severi,  
719 S., Van Hoof, C., Musa, S., Van Helleputte, N., Yazicioglu, R. F., and Mitra, S. (2017). A Neural Probe With  
720 Up to 966 Electrodes and Up to 384 Configurable Channels in 0.13  $\mu\text{m}$  SOI CMOS. *IEEE TRANSACTIONS  
721 ON BIOMEDICAL CIRCUITS AND SYSTEMS*, 11(3):510–522.
- 722 Magland, J., Jun, J. J., Lovero, E., Morley, A. J., Hurwitz, C. L., Buccino, A. P., Garcia, S., and Barnett, A. H.  
723 (2020). SpikeForest, reproducible web-facing ground-truth validation of automated neural spike sorters.  
724 *eLife*, 9:e55167, ISSN: 2050–084X, DOI: [10.7554/eLife.55167](https://doi.org/10.7554/eLife.55167).
- 725 Müller, J., Ballini, M., Livi, P., Chen, Y., Radivojevic, M., Shadmani, A., Viswam, V., Jones, I. L., Fiscella,  
726 M., Diggelmann, R., Stettler, A., Frey, U., Bakkum, D. J., and Hierlemann, A. (2015). High-resolution  
727 CMOS MEA platform to study neurons at subcellular, cellular, and network levels. *Lab on a Chip*,  
728 15(13):2767–2780, ISSN: 1473–0197, 1473–0189, DOI: [10.1039/C5LC00133A](https://doi.org/10.1039/C5LC00133A), <http://xlink.rsc.org/?DOI=C5LC00133A>.  
729
- 730 Obien, M. E. J., Deligkaris, K., Bullmann, T., Bakkum, D. J., and Frey, U. (2015). Revealing  
731 neuronal function through microelectrode array recordings. *Frontiers in Neuroscience*, 8, ISSN:  
732 1662–453X, DOI: [10.3389/fnins.2014.00423](https://doi.org/10.3389/fnins.2014.00423), <http://journal.frontiersin.org/article/10.3389/fnins.2014.00423/abstract>.  
733
- 734 Olsson, R. H. and Wise, K. D. (2005). A three-dimensional neural recording microsystem with implantable  
735 data compression circuitry. *IEEE Journal of Solid-State Circuits*, 40(12):2796–2804, ISSN: 1558–173X, DOI:  
736 [10.1109/JSSC.2005.858479](https://doi.org/10.1109/JSSC.2005.858479).
- 737 Pachitariu, M., Steinmetz, N. A., Kadir, S. N., Carandini, M., and Harris, K. D. (2016). Fast and ac-  
738 curate spike sorting of high-channel count probes with KiloSort. *Advances in Neural Information  
739 Processing Systems*, 29(Nips):4448–4456, ISSN: 10495258, [https://papers.nips.cc/paper/  
740 6326-fast-and-accurate-spike-sorting-of-high-channel-count-probes-with-kilosort.pdf](https://papers.nips.cc/paper/6326-fast-and-accurate-spike-sorting-of-high-channel-count-probes-with-kilosort.pdf).  
741

- 742 Raducanu, B. C., Yazicioglu, R. F., Lopez, C. M., Ballini, M., Putzeys, J., Wang, S., Andrei, A., Rochus, V.,  
743 Welkenhuysen, M., van Helleputte, N., Musa, S., Puers, R., Kloosterman, F., van Hoof, C., Fiáth, R., Ulbert,  
744 I., and Mitra, S. (2017). Time Multiplexed Active Neural Probe with 1356 Parallel Recording Sites. *Sensors*,  
745 17(10):2388, DOI: [10.3390/s17102388](https://doi.org/10.3390/s17102388).
- 746 Rios, G., Lubenov, E. V., Chi, D., Roukes, M. L., and Siapas, A. G. (2016). Nanofabricated Neural  
747 Probes for Dense 3-D Recordings of Brain Activity. *Nano Letters*, 16(11):6857–6862, ISSN: 1530–6984,  
748 1530–6992, DOI: [10.1021/acs.nanolett.6b02673](https://doi.org/10.1021/acs.nanolett.6b02673), <https://pubs.acs.org/doi/10.1021/acs.nanolett.6b02673>.
- 750 Robinson, D. (1968). The electrical properties of metal microelectrodes. *Proceedings of the IEEE*, 56(6):1065–  
751 1071, ISSN: 0018–9219, DOI: [10.1109/PROC.1968.6458](https://doi.org/10.1109/PROC.1968.6458), <http://ieeexplore.ieee.org/document/1448388/>.
- 753 Schomburg, E. W., Anastassiou, C. A., Buzsáki, G., and Koch, C. (2012). The Spiking Component of Oscilla-  
754 tory Extracellular Potentials in the Rat Hippocampus. *Journal of Neuroscience*, 32(34):11798–11811, ISSN:  
755 0270–6474, 1529–2401, DOI: [10.1523/JNEUROSCI.0656-12.2012](https://doi.org/10.1523/JNEUROSCI.0656-12.2012).
- 756 Seidl, K., Herwik, S., Torfs, T., Neves, H., Paul, O., and Ruther, P. (2011). CMOS-Based High-Density Silicon  
757 Microprobe Arrays for Electronic Depth Control in Intracortical Neural Recording. *Journal of Microelec-*  
758 *tromechanical Systems*, 20:1439–1448.
- 759 Seidl, K., Schwaerzle, M., Ulbert, I., Neves, H. P., Paul, O., and Ruther, P. (2012). CMOS-Based  
760 High-Density Silicon Microprobe Arrays for Electronic Depth Control in Intracortical Neural Record-  
761 ing–Characterization and Application. *Journal of Microelectromechanical Systems*, 21(6):1426–1435,  
762 ISSN: 1057–7157, 1941–0158, DOI: [10.1109/JMEMS.2012.2206564](https://doi.org/10.1109/JMEMS.2012.2206564), <http://ieeexplore.ieee.org/document/6249712/>.
- 764 Shahrokhi, F., Abdelhalim, K., Serletis, D., Carlen, P. L., and Genov, R. (2010). The 128-Channel Fully Differ-  
765 ential Digital Integrated Neural Recording and Stimulation Interface. *IEEE Transactions on Biomedical Cir-*  
766 *cuits and Systems*, 4(3):149–161, ISSN: 1932–4545, 1940–9990, DOI: [10.1109/TBCAS.2010.2041350](https://doi.org/10.1109/TBCAS.2010.2041350),  
767 <http://ieeexplore.ieee.org/document/5471738/>.
- 768 Shannon, C. E. (1949). Communication in the Presence of Noise. *Proceedings of the IRE*, 37(1):10–21, ISSN:  
769 0096–8390, DOI: [10.1109/JRPROC.1949.232969](https://doi.org/10.1109/JRPROC.1949.232969).
- 770 Siegle, J. H., Jia, X., Durand, S., Gale, S., Bennett, C., Graddis, N., Heller, G., Ramirez, T. K., Choi, H., Luviano,  
771 J. A., Groblewski, P. A., Ahmed, R., Arkhipov, A., Bernard, A., Billeh, Y. N., Brown, D., Buice, M. A., Cain, N.,  
772 Caldejon, S., Casal, L., Cho, A., Chvilicek, M., Cox, T. C., Dai, K., Denman, D. J., de Vries, S. E. J., Dietzman,  
773 R., Esposito, L., Farrell, C., Feng, D., Galbraith, J., Garrett, M., Gelfand, E. C., Hancock, N., Harris, J. A.,  
774 Howard, R., Hu, B., Hytinen, R., Iyer, R., Jessett, E., Johnson, K., Kato, I., Kiggins, J., Lambert, S., Lecoq,  
775 J., Ledochowitsch, P., Lee, J. H., Leon, A., Li, Y., Liang, E., Long, F., Mace, K., Melchior, J., Millman, D.,  
776 Mollenkopf, T., Nayan, C., Ng, L., Ngo, K., Nguyen, T., Nicovich, P. R., North, K., Ocker, G. K., Ollerenshaw,  
777 D., Oliver, M., Pachitariu, M., Perkins, J., Reding, M., Reid, D., Robertson, M., Ronellenfitch, K., Seid, S.,  
778 Slaughterbeck, C., Stoecklin, M., Sullivan, D., Sutton, B., Swapp, J., Thompson, C., Turner, K., Wakeman,  
779 W., Whitesell, J. D., Williams, D., Williford, A., Young, R., Zeng, H., Naylor, S., Phillips, J. W., Reid, R. C.,  
780 Mihalas, S., Olsen, S. R., and Koch, C. (2019). A survey of spiking activity reveals a functional hierarchy  
781 of mouse corticothalamic visual areas. *bioRxiv*, DOI: [10.1101/805010](https://doi.org/10.1101/805010), <https://www.biorxiv.org/content/early/2019/10/16/805010>.
- 783 Steinmetz, N. A., Aydin, C., Lebedeva, A., Okun, M., Pachitariu, M., Bauza, M., Beau, M., Bhagat, J., Böhm, C.,

- 784 Broux, M., Chen, S., Colonell, J., Gardner, R. J., Karsh, B., Kloosterman, F., Kostadinov, D., Mora-Lopez, C.,  
785 O'Callaghan, J., Park, J., Putzeys, J., Sauerbrei, B., van Daal, R. J. J., Vollan, A. Z., Wang, S., Welkenhuysen,  
786 M., Ye, Z., Dudman, J. T., Dutta, B., Hantman, A. W., Harris, K. D., Lee, A. K., Moser, E. I., O'Keefe, J.,  
787 Renart, A., Svoboda, K., Häusser, M., Haesler, S., Carandini, M., and Harris, T. D. (2021). Neuropixels  
788 2.0: A miniaturized high-density probe for stable, long-term brain recordings. *Science*, 372(6539), ISSN:  
789 0036-8075, 1095-9203, DOI: [10.1126/science.abf4588](https://doi.org/10.1126/science.abf4588).
- 790 Stevenson, I. (2013). Tracking Advances in Neural Recording | Statistical Neuroscience Lab.  
791 <https://stevenson.lab.uconn.edu/scaling/>.
- 792 Stringer, C., Pachitariu, M., Steinmetz, N., Reddy, C. B., Carandini, M., and Harris, K. D. (2019). Sponta-  
793 neous behaviors drive multidimensional, brainwide activity. *Science*, 364(6437), ISSN: 0036-8075, DOI:  
794 [10.1126/science.aav7893](https://doi.org/10.1126/science.aav7893), <https://science.sciencemag.org/content/364/6437/eaav7893>.
- 795 Suo, Y., Zhang, J., Xiong, T., Chin, P. S., Etienne-Cummings, R., and Tran, T. D. (2014). Energy-Efficient Multi-  
796 Mode Compressed Sensing System for Implantable Neural Recordings. *Ieee Transactions on Biomedical*  
797 *Circuits and Systems*, 8(5):648-659, ISSN: 1932-4545, DOI: [10.1109/TBCAS.2014.2359180](https://doi.org/10.1109/TBCAS.2014.2359180).
- 798 Torfs, T., Aarts, A., Erismis, M. A., Aslam, J., Yazicioglu, R. F., Puers, R., Van Hoof, C., Neves, H., Ul-  
799 bert, I., Dombovari, B., Fiath, R., Kerekes, B. P., Seidl, K., Herwik, S., and Ruther, P. (2010). Two-  
800 dimensional multi-channel neural probes with electronic depth control. In *2010 Biomedical Circuits and*  
801 *Systems Conference (BioCAS)*, pages 198-201, Paphos, Cyprus. IEEE, ISBN: 978-1-4244-7269-7, DOI:  
802 [10.1109/BIOCAS.2010.5709605](https://doi.org/10.1109/BIOCAS.2010.5709605), <http://ieeexplore.ieee.org/document/5709605/>.
- 803 Yger, P., Spampinato, G. L., Esposito, E., Lefebvre, B., Deny, S., Gardella, C., Stimberg, M., Jetter, F., Zeck,  
804 G., Picaud, S., Duebel, J., and Marre, O. (2018). A spike sorting toolbox for up to thousands of elec-  
805 trodes validated with ground truth recordings in vitro and in vivo. *eLife*, 7, ISSN: 2050-084X, DOI:  
806 [10.7554/eLife.34518](https://doi.org/10.7554/eLife.34518).